

Convective-scale perturbation growth across the spectrum of convective regimes

Article

Accepted Version

Flack, D. L. A., Gray, S. L., Plant, R. S., Lean, H. W. and Craig, G. C. (2017) Convective-scale perturbation growth across the spectrum of convective regimes. *Monthly Weather Review*. ISSN 0027-0644 (In Press) Available at <http://centaur.reading.ac.uk/74117/>

It is advisable to refer to the publisher's version if you intend to cite from the work.

Publisher: American Meteorological Society

All outputs in CentAUR are protected by Intellectual Property Rights law, including copyright law. Copyright and IPR is retained by the creators or other copyright holders. Terms and conditions for use of this material are defined in the [End User Agreement](#).

www.reading.ac.uk/centaur

CentAUR

Central Archive at the University of Reading

Reading's research outputs online

1 **Convective-Scale Perturbation Growth Across the Spectrum of Convective**
2 **Regimes**

3 David L. A. Flack*, Suzanne L. Gray and Robert S. Plant

4 *Department of Meteorology, University of Reading, Reading, UK.*

5 Humphrey W. Lean

6 *MetOffice@Reading, University of Reading, Reading, UK*

7 George C. Craig

8 *Meteorologisches Institut, Ludwig-Maximilians-Universität München, München, Germany*

9 *Corresponding author address: D. L. A. Flack, Department of Meteorology, University of Read-
10 ing, Earley Gate, PO Box 243, Reading, RG6 6BB, UK.

11 E-mail: d.l.a.flack@reading.ac.uk

ABSTRACT

12 Convection-permitting ensembles have led to improved forecasts of many
13 atmospheric phenomena. However, to fully utilize these forecasts the depen-
14 dence of predictability on synoptic conditions needs to be understood. In
15 this study, convective regimes are diagnosed based on a convective timescale
16 which identifies the degree to which convection is in equilibrium with the
17 large-scale forcing. Six convective cases are examined in a convection-
18 permitting ensemble constructed using the Met Office Unified Model. The
19 ensemble members were generated using small-amplitude buoyancy pertur-
20 bations added into the boundary layer, which can be considered to represent
21 turbulent fluctuations close to the gridscale. Perturbation growth is shown
22 to occur on different scales with an order of magnitude difference between
23 the regimes ($O(1\text{ km})$ for cases closer to non-equilibrium convection and
24 $O(10\text{ km})$ for cases closer to equilibrium convection). This difference reflects
25 the fact that cell locations are essentially random in the equilibrium events af-
26 ter the first 12 h of the forecast, indicating a more rapid upscale perturbation
27 growth compared to the non-equilibrium events. Furthermore, large tempo-
28 ral variability is exhibited in all perturbation growth diagnostics for the non-
29 equilibrium regime. Two boundary condition driven cases are also considered
30 and show similar characteristics to the non-equilibrium cases, implying that
31 caution is needed to interpret the timescale when initiation is not within the
32 domain. Further understanding of perturbation growth within the different
33 regimes could lead to a better understanding of where ensemble design im-
34 provements can be made beyond increasing the model resolution and could
35 improve interpretation of forecasts.

36 **1. Introduction**

37 Convection-permitting numerical weather prediction (NWP) models have led to improved fore-
38 casts of many atmospheric phenomena (e.g. fog and low cloud; convective precipitation; tropical
39 cyclone intensity and tracks: McCabe et al. 2016; Clark et al. 2016; Xue et al. 2013). However,
40 the atmosphere is chaotic and error growth is faster at smaller scales (Lorenz 1969). Therefore,
41 increasing the resolution of an NWP model will result in faster error growth. For example, Ho-
42 henegger and Schär (2007a) found an order of magnitude difference between error doubling times
43 when comparing a convection-permitting model (grid length: 2.2 km) with a coarser-resolution,
44 convection-parametrizing model (grid length: 80 km). Rapid error growth implies more limited
45 intrinsic predictability (defined as how predictable a situation is assuming an optimal forecast
46 (Lorenz 1969) with near-perfect initial conditions and perfect boundary conditions) on convective
47 scales (e.g. Hohenegger et al. 2006; Clark et al. 2009, 2010). The predictability of convection-
48 permitting models remains an active area of research (e.g. Melhauser and Zhang 2012; Johnson
49 and Wang 2016), important for both the modeling and forecasting communities. Several studies
50 have shown that the predictability of precipitation depends, in part, upon whether the convection
51 is predominantly controlled by large-scale or local factors (e.g. Done et al. 2006; Keil and Craig
52 2011; Kühnlein et al. 2014). Important aspects of convective-scale predictability include the tim-
53 ing (which is better captured with increasing resolution; Lean et al. 2008) and spatial positioning
54 of convection.

55 The spatial variability of precipitation within convection-permitting forecasts has led to issues
56 with their verification. Mittermaier (2014) provides a review of these issues and of appropriate ver-
57 ification techniques. Analyses with scale-dependent techniques such as the Fractions Skill Score
58 (FSS; Roberts and Lean 2008) have shown wide variations in the ability of models to forecast the

59 locations of convective events. For example, a peninsula convergence line in the south west of the
60 United Kingdom on 3 August 2013 was forecast operationally with a high degree of spatial agree-
61 ment between ensemble members close to the gridscale (i.e., predictable), whereas a convective
62 event in the east of the UK on the previous day was poorly forecast with weak spatial agreement
63 between ensemble members (Dey et al. 2016).

64 The growth and development of small-scale errors in convective-scale forecasts has been con-
65 sidered in various studies. Surcel et al. (2016) considered the locality of perturbation growth and
66 showed that more widespread precipitation was associated with marginally better predictability at
67 synoptic scales, but similar predictability to diurnally-forced cases at smaller scales. Studies such
68 as Zhang et al. (2007) and Selz and Craig (2015) have examined upscale error growth and found
69 that an initial phase of rapid exponential error growth at the convective scale is linked to variations
70 in the convective mass flux. Johnson et al. (2014) considered multi-scale interactions to show that
71 the growth with the largest energy occurred at wavelengths of around 30–60 km. All of these pre-
72 vious studies indicate a strong association between convection and error growth. However, they
73 did not establish how such growth might depend on the character of the convection¹.

74 Convection can be classified as occurring in a spectrum between two main regimes. One regime
75 is convective quasi-equilibrium in which the large-scale production of instability is balanced by
76 its release at the convective scale, typical for cases with large-scale synoptic uplift (Arakawa and
77 Schubert 1974). The convection associated with this regime is often in the form of scattered
78 showers and typically has limited spatial organization. The second regime is non-equilibrium con-
79 vection. This regime occurs when there is a build-up of convective instability facilitated by some

¹In fact, Surcel et al. (2016) did look for dependencies on a convective timescale, computed as $CAPE/(dCAPE/dt)$, the denominator being estimated from a finite difference of CAPE values. They found no link between this timescale and differences in perturbation growth. However, it is important to recognize that their timescale is *not* the same as the adjustment timescale as defined in (1) and as used throughout the present article.

80 inhibiting factor. If this factor can be overcome then the convective instability is released. These
 81 types of events are more often associated with more organized forms of convection (Emanuel
 82 1994). To distinguish between the regimes the convective adjustment timescale, τ_c , may be used.
 83 This timescale was introduced by Done et al. (2006) and is defined as the ratio between the Con-
 84 vective Available Potential Energy (CAPE) and its rate of release at the convective scale (subscript
 85 CS):

$$\tau_c = \frac{CAPE}{|dCAPE/dt|_{CS}}. \quad (1)$$

86 The rate of release can be estimated based upon the latent heat release from precipitation, leading
 87 to

$$\tau_c = \frac{1}{2} \frac{c_p \rho_0 T_0}{L_v g} \frac{CAPE}{P}, \quad (2)$$

88 where c_p is the specific heat capacity at constant pressure, ρ_0 and T_0 are a reference density (1.2
 89 kg m⁻³) and temperature (273.15 K) respectively, L_v is the latent heat due to vaporization, g is
 90 the acceleration due to gravity and P is the precipitation rate (which is best estimated from an
 91 accumulation over 1–3 hours rather than an instantaneous precipitation rate: Flack et al. (2016)).
 92 The factor of a half was introduced by Molini et al. (2011) to account for factors such as boundary
 93 layer modification, the neglect of which would lead to an overestimation of τ_c (Keil and Craig
 94 2011). The convective adjustment timescale has been used in this study as an indicator of the
 95 convective regime. The threshold between the equilibrium and non-equilibrium regime occurs in
 96 the range of 3–12 h (Zimmer et al. 2011).

97 As previously shown (e.g. Done et al. 2006; Keil and Craig 2011; Zimmer et al. 2011; Craig
 98 et al. 2012; Flack et al. 2016) the value of τ_c should be used to indicate the likely nature of the
 99 regime, rather than to definitively classify it. The timescale can be a particularly useful indicator
 100 at the onset of convection (when the event starts to precipitate), but is likely to reduce in value as

101 convection develops further, particularly in non-equilibrium cases which are often long lived (e.g.
102 Molini et al. 2011). The extent to which τ_c reduces either in time (e.g. Done et al. 2006) or with
103 distance from the forcing region (e.g. Flack et al. 2016) depends on the event. The timescale is
104 a particularly useful diagnostic if the value is far from the threshold. However, in practice τ_c can
105 be close to the threshold. In such situations additional information (such as inspection of synoptic
106 charts) may be necessary to help determine the character of a given event, or else it should be
107 recognized that the event may be intermediate in character.

108 The convective adjustment timescale has been used for many purposes (e.g. Done et al. 2006;
109 Molini et al. 2011; Done et al. 2012). Climatologies have been produced, based on observations
110 over Germany (Zimmer et al. 2011) and model output over the UK (Flack et al. 2016). One of
111 its key uses has been to consider the predictability of convection. Done et al. (2006) considered
112 two MCSs over the UK and found that the total area-averaged precipitation was similar for all
113 ensemble members in the equilibrium case and exhibited more spread for the non-equilibrium case.
114 This regime dependence of precipitation spread was confirmed for other equilibrium and non-
115 equilibrium cases by Keil and Craig (2011). Moreover, Keil et al. (2014) demonstrated that non-
116 equilibrium cases were more sensitive to model physics perturbations compared to equilibrium
117 cases. A similar contrast in the sensitivity was demonstrated for initial condition perturbations by
118 Kühnlein et al. (2014), who further showed a relative insensitivity to variations in lateral boundary
119 conditions. Their results are also consistent with Craig et al. (2012), who suggested that non-
120 equilibrium conditions are more sensitive to initial condition perturbations produced by radar data
121 assimilation: the assimilation has longer-lasting benefits for the forecasts in cases with longer τ_c .

122 In this study we apply small boundary-layer temperature perturbations in a controlled series
123 of experiments to assess the intrinsic predictability of convection in different regimes using a
124 selection of UK case studies. The case studies are chosen to cover a spectrum of τ_c and so sample

125 over the convective regimes. We primarily focus on the magnitude and spatial characteristics
126 of the perturbation growth as a greater understanding of the spatial predictability of convective
127 events in various situations could lead to improved forecasts of flooding from intense rainfall
128 events through improved modeling strategy or interpretation of forecasts. This focus is achieved
129 by testing the following hypotheses: (i) there is faster initial perturbation growth in convective
130 quasi-equilibrium compared to non-equilibrium and (ii) due to the association of convection with
131 explicit triggering mechanisms in the non-equilibrium regime (Done et al. 2006), perturbation
132 growth will be relatively localized for non-equilibrium convection but more widespread for events
133 in convective quasi-equilibrium.

134 The rest of this paper is structured as follows: the ensembles and diagnostics are discussed in
135 Section 2; the cases considered are outlined in Section 3; the perturbation growth characteristics
136 are examined in Section 4; and conclusions and discussion are presented in Section 5.

137 **2. Methodology**

138 Ensembles have been run for six case studies labeled A to F (Section 3). The model and control
139 run are described first (Section 2a), followed by the perturbation strategy (Section 2b) and the
140 diagnostics (Section 2c).

141 *a. Model*

142 The Met Office Unified Model (MetUM), version 8.2, has been used in this study. This version
143 was operational in summer 2013 and produced forecasts for all but one of the cases examined.
144 The dynamical core of the MetUM is semi-implicit, semi-Lagrangian and non-hydrostatic. More
145 details of the dynamical core of the version used in this study are described by Davies et al.

146 (2005)². The MetUM has parametrizations for unresolved processes including a microphysics
147 scheme adapted from Wilson and Ballard (1999), the Lock et al. (2000) boundary layer scheme, the
148 Best et al. (2011) surface layer scheme, and the Edwards and Slingo (1996) radiation scheme. No
149 convection parametrization is used for this study. The ensembles use the United Kingdom Variable
150 resolution (UKV) configuration, which has a horizontal grid length of 1.5 km in the interior domain
151 and so is classed as convection permitting (Clark et al. 2016). The variable resolution part of the
152 configuration occurs only towards the edges of the domain, where the grid length ranges from 4 to
153 1.5 km (Tang et al. 2013). The vertical extent of the model is 40 km, and its 70 levels are stretched
154 such that the resolution is greatest in the boundary layer.

155 The 36-hour simulations performed here are initialized from the Met Office global analysis
156 (grid length 25 km) at 0000 UTC on the day of the event. All simulations have a spin-up time
157 of three hours (estimated from temporal cross-correlations of hourly precipitation accumulations
158 between the control and perturbed forecasts of the same ensemble, not shown) associated with
159 the downscaling of coarser-resolution initial conditions. Therefore the analysis is restricted to the
160 last 33 h of the ensemble forecasts. It is expected that the impact of spin-up will be significantly
161 reduced after this time in comparison to the perturbation growth.

162 *b. Perturbation Strategy*

163 Perturbations have been applied on a single vertical level to create six-member ensembles for
164 each of the cases. These perturbations are applied within the boundary layer across the entire
165 horizontal domain and are based upon the formulation of Leoncini et al. (2010) and Done et al.
166 (2012):

$$\text{perturbation}(x, y) = A \exp \left[-\frac{(x - x_0)^2 + (y - y_0)^2}{2\sigma^2} \right],$$

²The operational dynamical core of the MetUM has since changed to the Even Newer Dynamics (Wood et al. 2014).

167 for A the amplitude of the perturbation, x the position in the zonal direction, y the position in the
168 meridional direction, (x_0, y_0) the central position of the Gaussian distribution, and σ the standard
169 deviation which determines the spatial scale of the perturbations. The amplitude is initially set
170 to random values uniformly distributed between ± 1 . A superposition of Gaussian distributions is
171 created by centering Gaussian distributions at every grid point in the domain. This result is scaled
172 to an appropriate amplitude for the total perturbation as in Leoncini et al. (2010) and Done et al.
173 (2012). Here the perturbation field is added to potential temperature and scaled for a maximum
174 amplitude of 0.1 K. Such an amplitude is typical of potential temperature variations within the
175 convective boundary layer (e.g. Wyngaard and Cot 1971). Based on the perturbation amplitude
176 experiments in Leoncini et al. (2010) (and sensitivity experiments performed for this study; not
177 shown), increasing the amplitude of the perturbation would increase the initial growth of differ-
178 ences between runs but would not significantly change the saturation level of the differences.

179 The standard deviation used is 9 km, a distance of $6\Delta x$, for which the UKV configuration can be
180 expected to reasonably resolve atmospheric phenomena and orography (e.g. Bierdel et al. 2012;
181 Verrelle et al. 2015). The perturbations are designed to represent variability in turbulent fluxes
182 that cannot be fully resolved by the model (via stochastic forcing), and are hence randomized
183 each time they are applied. They are applied once every 15 minutes, throughout the forecast,
184 corresponding to around half a typical eddy turnover time for a convective boundary layer (Byers
185 and Braham 1948). The perturbations are applied at a model hybrid height of 261.6 m. This height
186 is consistently within the boundary layer throughout the entire forecast on all days considered (not
187 shown), but outside the surface layer to reduce modification by friction and other surface effects.

188 The perturbation approach is simplistic, and is not designed for use on its own in generating
189 operational ensembles, However, it is sufficient to allow for effective perturbation growth at the
190 convective scale (e.g. Raynaud and Bouttier 2015) and it keeps the synoptic situation indistin-

191 guishable from the control. Thus differences in the intensity and position of convection between
192 ensemble members are solely due to these perturbations. This is a different ensemble generation
193 method to that used for the operational convection-permitting ensemble at the Met Office. The
194 operational ensemble uses downscaled initial and boundary conditions from the global ensemble
195 that modify the synoptic conditions (Bowler et al. 2008, 2009). Recent additions to the operational
196 ensemble include random noise, although this is tiled across the domain rather than continuously
197 varying across the domain as in our experiments.

198 The sensitivity of the results to the perturbation strategy has also been tested for perturbations
199 applied on multiple levels and for spatially-correlated potential temperature and specific humidity
200 perturbations. The sensitivity tests result in similar behavior to the results presented here (Flack
201 2017, Chapter 6). The use of multiple-level perturbations, rather than single-level perturbations,
202 had no discernible impact on any of the results because the perturbations are immediately pro-
203 cessed by the boundary layer scheme and so spread in the vertical before numerical dissipation
204 in the advection scheme can act to dampen their magnitude. The inclusion of spatially-correlated
205 moisture perturbations resulted in marginally-faster initial perturbation growth only.

206 *c. Diagnostics*

207 Diagnostics have been considered that take into account both the magnitude and spatial context
208 of the perturbation growth. These are described here.

209 1) CONVECTIVE ADJUSTMENT TIMESCALE

210 The convective adjustment timescale, calculated from the control forecast, is used to indicate
211 where the case studies lie on the spectrum between the equilibrium and non-equilibrium regimes.
212 For this study a spatial average across the domain, for only the points where τ_c is defined, is used

213 alongside hourly averaged τ_c maps. The method to calculate τ_c is summarized here; justification
214 and full details are presented in Flack et al. (2016), and sensitivity tests are shown in Chapter 3 of
215 Flack (2017). These sensitivity tests implied that using precipitation accumulations resulted in a
216 timescale that was less spatially noisy (implying clearer regime classification) compared to when
217 instantaneous precipitation rates were used.

218 The method uses a Gaussian kernel, with a half-width of 60 km, to smooth the coarse-grained
219 hourly precipitation accumulations (converted into average precipitation rates) and the CAPE be-
220 fore (2) is then evaluated. The half-width is chosen to lie between typical cloud-separation dis-
221 tances and the synoptic scale, and for consistency with other studies (e.g. Keil and Craig 2011). A
222 precipitation threshold of 0.2 mm h^{-1} is applied to the precipitation field after the Gaussian kernel
223 has been applied. The precipitation threshold is chosen to limit stratiform rain but to allow for a
224 meaningful sample of precipitating points in the domain. The hourly model data is used to provide
225 a higher temporal resolution of τ_c compared to Flack et al. (2016).

226 Should the spatially-averaged τ_c for an event be clearly distinct from 3 hours (i.e. not within 2–4
227 h) then the regime is classed as being towards the non-equilibrium end of the spectrum (clearly
228 above 3 hours) or towards the equilibrium end of the spectrum (clearly below 3 hours). This 3-
229 hour threshold is chosen based on the climatology over the UK presented in Flack et al. (2016)
230 which indicated a distinct scale break in the τ_c spectrum at around 3 hours. As discussed in the
231 introduction, caution should be exercised in the use of τ_c for intermediate values close to the
232 threshold. Synoptic charts are therefore also considered when characterizing the studied events in
233 Section 3.

234 2) MEAN SQUARE DIFFERENCE

235 The Mean Square Difference (MSD) is a simple and effective measure for considering the spread
236 of an ensemble, and has been used for many years at the convective scale (e.g. Hohenegger et al.
237 2006; Hohenegger and Schär 2007a,b; Clark et al. 2009; Leoncini et al. 2010, 2013; Johnson et al.
238 2014). It is given by

$$MSD = \gamma_{\chi} \sum (\chi_p - \chi_c)^2, \quad (3)$$

239 for χ_p a variable in the perturbed forecast and χ_c the same variable in the control forecast, γ_{χ} is a
240 normalization factor that depends on the variable considered.

241 In this study, MSD has been calculated for two variables: the temperature on a model level
242 in the lower free troposphere (on the model level closest to 850 hPa) and hourly accumulations
243 of precipitation exceeding 1 mm (an arbitrary threshold for convective precipitation). When the
244 temperature is being used the normalization factor is simply the reciprocal of the number of grid
245 points in the domain, N , i.e. $\gamma_T = 1/N$.

246 The MSD is a grid-point quantity and so is subject to the “double penalty” problem (Roberts
247 and Lean 2008) when applied to precipitation at convection-permitting scales. This problem oc-
248 curs when a forecast is penalized twice for having precipitation in the wrong position: once for
249 forecasting precipitation that is not observed and once for failing to forecast observed precipita-
250 tion. This can complicate the interpretation of MSD. Here, we wish to use the precipitation MSD
251 as a measure of changes in precipitation rates, and hence it is calculated only from those points
252 where the hourly accumulation exceeds 1 mm in both the perturbed and control forecasts. So
253 that the results are robust to total precipitation, to enable fair comparisons across the case studies
254 considered, the normalization factor considers the total precipitation from all points in the control

255 forecast that exceed the threshold. Hence,

$$\gamma_P = \frac{1}{\sum P_c^2}$$

256 for P_c the hourly-precipitation accumulation in the control forecast.

257 3) FRACTION OF COMMON POINTS

258 The number of common points, N_{12} , is defined as the number of points that exceed an hourly-
259 precipitation accumulation of 1 mm in two different forecasts for the same event (be it a control-
260 member or member-member comparison). This allows the fraction of common points (F_{common})
261 to be defined as the ratio of the number of common points to the total number of precipitating
262 points (i.e., the total number of precipitating points in the first forecast, N_1 , plus the total number
263 of precipitating points in the second forecast, N_2 , minus the number of common points between
264 both forecasts as to eliminate double counting):

$$F_{common} = \frac{N_{12}}{N_1 + N_2 - N_{12}}. \quad (4)$$

265 F_{common} varies between zero and unity, where a value of unity implies two forecasts that are spa-
266 tially identical and zero implies no common points.

267 4) FRACTIONS SKILL SCORE

268 The FSS was introduced by Roberts and Lean (2008) to combat the “double penalty” problem.
269 It is a neighborhood-based technique (Ebert 2008) used for verification and is given by

$$FSS = 1 - \frac{\sum (f - o)^2}{\sum f^2 + \sum o^2},$$

270 where f represents the fraction of points with precipitation over a specified threshold in the fore-
271 cast (perturbed member in our case) and o represents the fraction of points with precipitation
272 over the same threshold in the observations (control forecast in our case). Here a threshold of

273 hourly-precipitation accumulations exceeding 1 mm is applied. The FSS can be adapted to con-
274 sider ensemble spread by considering the mean over FSS differences between pairs of perturbed
275 ensemble members, as proposed by Dey et al. (2014). This gives rise to the dispersive FSS (dFSS)
276 which can be used as a tool for considering the predictability of convection (e.g. Johnson and
277 Wang 2016).

278 The FSS ranges between zero (forecasts completely different spatially) and unity (forecasts spa-
279 tially identical). The distinction between a skillful forecast (with respect to either observations
280 or to a different ensemble member) and a less skillful forecast is considered to occur at a value
281 of 0.5 (Roberts and Lean 2008). Although it provides information about the spatial structure of
282 perturbation growth, the FSS does not provide information about the perturbation magnitude.

283 **3. Case Studies**

284 A set of case studies is examined that covers a spectrum of τ_c . This spectrum enables a pic-
285 ture to emerge of the differences between the regimes in real scenarios. Four of the cases (A–D)
286 are presented in order from that closest to convective quasi-equilibrium (A) to that furthest from
287 equilibrium (D). Cases A–D are classified based on a combination of Figs. 1–4. Figure 1 is the op-
288 erational surface analysis at 1200 UTC on the day of the convective event; Fig. 2 shows the number
289 of ensemble members that are producing precipitation; Fig. 3 is the evolution of τ_c throughout the
290 forecast, and Fig. 4 shows maps of τ_c at 1500 UTC. This time is selected as convective precipita-
291 tion is well established in all of the forecasts and to indicate the differences in regime classification
292 despite the similarity in the spatially-averaged timescale. The other two cases (E and F) consider
293 convection initiated outside of the domain, which is another scenario of importance for convective-
294 scale modeling.

295 *a. Case A: 20 April 2012*

296 This case was part of the DYNAmical and Microphysical Evolution of Convective Storms
297 (DYMECS) field experiment (Stein et al. 2015) and shows typical conditions for scattered show-
298 ers in the UK, which initiated at 1000 UTC. The 1200 UTC synoptic chart (Fig. 1a) shows the
299 situation that was present throughout the entire forecast. There was a low pressure center situated
300 in the north east of the UK and several troughs over the country. Furthermore, the UK was posi-
301 tioned to the left of the tropopause-level jet exit (Fig. 3.5 of Flack 2017), implying synoptic-scale
302 uplift. The presence of large-scale forcing suggests that this case is likely to be in convective
303 quasi-equilibrium. The different ensemble members produce showers in different positions (the
304 number of ensemble members with precipitation in the same position is indicated in Fig. 2a),
305 but have a consistent domain-average precipitation throughout the forecast with close agreement
306 between the perturbed members and the control (Fig. 5); this result is in agreement with the equi-
307 librium cases considered by Done et al. (2006, 2012) and Keil and Craig (2011). The hypothesis
308 that this event should be placed near the equilibrium end of the spectrum is supported by τ_c being
309 consistently below the three-hour threshold throughout the forecast both temporally (Fig. 3) and
310 spatially (Fig. 4a). This case is thus put towards the equilibrium end of the spectrum considered.

311 *b. Case B: 12 August 2013*

312 In this case a surface low was situated over Scandinavia and the Azores high was beginning to
313 build (Fig. 1b), leading to persistent north-westerly flow. An upper-level cold front trailed a weak
314 surface front and there was a trough passing over Scotland that provided large-scale synoptic
315 uplift, suggesting an equilibrium-regime day. The showers associated with this day initiated at
316 1100 UTC. The average rainfall is approximately constant at around 0.3 mm h^{-1} throughout the
317 forecast (Fig. 5) and the ensemble members place the showers in different positions in the north

318 of the country, with very few showers in the south (Fig. 2b). The timescale is consistently close to
319 or below the threshold throughout the forecast period (Fig. 3) and there are no localized regions
320 of long timescales in the map (Fig. 4b). However, it is more intermediate than Case A, so is thus
321 a marginal-equilibrium event.

322 *c. Case C: 23 July 2013*

323 This case was the fifth Intensive Observation Period (IOP 5) of the Convective Precipitation
324 Experiment (COPE; Leon et al. 2016). A low pressure system was centered to the west of the UK
325 with several fronts ahead of the main center (Fig. 1c), that later decayed. The convection producing
326 the most precipitation on this day, associated with surface water flooding in Nottingham (in central
327 England; Nottingham City Council 2015), was ahead of these fronts and located along a surface
328 trough. There were several convective events forming along the surface trough, with some of them
329 producing intense precipitation (Fig. 5) and all tracking over similar regions. The first convection
330 on this day initiated at 0200 UTC, and there was a further burst of convection later in the day
331 initiating at 1500 UTC. The convective adjustment timescale (Fig. 3) showed initially long values,
332 which later decreased as the event matured as expected for non-equilibrium events (e.g. Done et al.
333 2006; Keil and Craig 2011; Flack et al. 2016). However, Fig. 3 indicates that the domain-average
334 τ_c , after spin-up, is around 2–3 hours for the majority of the forecast suggesting an intermediate
335 event. Synoptic analyses (Fig. 1c) do not suggest that a region of synoptic-scale forcing exists
336 and Fig. 4c shows localized regions of longer τ_c (exceeding three hours). These characteristics
337 are typically associated with non-equilibrium convective events and so this event is classified as a
338 marginal non-equilibrium event.

339 *d. Case D: 2 August 2013*

340 This case was IOP 10 of the COPE field campaign , with convection initiating at 1100 UTC. The
341 synoptic situation (Fig. 1d) shows a low pressure system centered to the west of Scotland, which
342 led to south-westerly winds and a convergence line being set up along the North Cornish coastline
343 (in southwest England). The convective cells that developed on this day were mainly associated
344 with this convergence line. The convective adjustment timescale remains above the three-hour
345 threshold for the majority of the forecast period (Fig. 3) and long τ_c are found over most of the
346 precipitating domain at the time shown in Fig. 4d. The domain-average precipitation (Fig. 5)
347 remains consistent between ensemble members. Due to the synoptic situation implying limited
348 synoptic-scale uplift around the convergence line, consistent long τ_c and consistent positioning of
349 precipitating cells (Fig. 2d), this case is classified as being towards the non-equilibrium end of the
350 spectrum.

351 *e. Case E: 27 July 2013*

352 This case was IOP 7 of the COPE field campaign. Two MCSs influenced the UK's weather
353 throughout the forecast period. The first MCS was situated over mainland Europe influencing the
354 Netherlands, Belgium and southeastern parts of the UK and is associated with the initial smaller
355 τ_c values in Fig. 3. The second MCS influenced the majority of UK. This second MCS entered the
356 model domain from the continent. However, unlike the previous MCS, it traveled north, across the
357 UK, during the forecast. As this MCS entered the domain it was associated with a long τ_c which
358 later reduced (being still associated with the same event); later still, as the MCS intensified in the
359 evening of 27 July, τ_c increased again (Fig. 3). The precipitation associated with the MCS led to
360 flooding in parts of Leicestershire (in central England; Leicestershire County Council 2014). The
361 heaviest precipitation was at approximately 1500 UTC when more stratiform rain was present, and

362 at 0300 UTC the following morning, when the MCS started to return south (Fig. 5). Throughout
363 the day there was persistent light southerly flow (Fig. 1e), with the UK being located in a region
364 with a weak pressure gradient. This synoptic situation, together with the long τ_c , would imply a
365 classification of this case towards the non-equilibrium end of the spectrum. However, as the MCS
366 has been advected into the domain rather than initiated within it, we instead classify Case E as
367 a case driven by the boundary conditions.

368 *f. Case F: 5 August 2013*

369 This case, IOP 12 of the COPE campaign, has been deliberately chosen as a complex situation
370 for considering convective-scale perturbation growth, and as a second case driven by the bound-
371 ary conditions. For the first 25 hours of the forecast a couple of fronts dominate the large-scale
372 situation (Fig. 1f). There is embedded convection associated with the fronts which led to localized
373 surface water flooding in Cornwall (in southwest England) (Cornwall Council 2015). There are
374 also showers ahead of the warm front near the Outer Hebrides (to the west of Scotland; Fig. 2f),
375 which dominate the precipitation after the front has cleared the UK. Figure 2f indicates that the
376 front is consistently positioned in the ensemble members, but the showers are inconsistently posi-
377 tioned. The total precipitation across the ensemble members remains fairly consistent throughout
378 the day after an initial heavy few hours (Fig. 5). Thus, Case F represents a transition from a
379 frontal regime to a convective regime driven by an evolving synoptic-scale flow, and most of the
380 convection passes into the domain through the boundary conditions.

381 **4. Results**

382 The perturbation growth for the spectrum of cases is examined in this section both in terms of
383 its magnitude (Section 4a) and spatial characteristics (Section 4b).

384 *a. Magnitude of Perturbation Growth*

385 We consider first whether the perturbation strategy employed induces biases in the perturbed
386 members with respect to the unperturbed control. Figure 5 indicates that whilst there is some
387 variation between the control forecast (solid lines) and the perturbed members (dashed lines) for a
388 given case, there are no major systematic differences between the forecasts. These computations
389 have also been performed using other precipitation thresholds (0.5 and 2 mm), with consistent
390 results (not shown). To confirm that the perturbed forecasts show no systematic bias with respect
391 to the control, a gamma distribution was fit to the probability density function of hourly accumu-
392 lations for each run and the shape and scale parameters were compared (not shown). The shape
393 and scale parameters indicate that the control lies within the spread of the perturbed members for
394 both parameters in all cases. This result was further confirmed through the use of a Mann-Whitney
395 U-test which indicates that the control and perturbed members are from a similar distribution at the
396 5% significance level. Combining the statistical tests with the visual similarity of the precipitation
397 distributions implies that, unlike the experiments of Kober and Craig (2016) for example, none of
398 our perturbed ensembles show any bias to the control. Differences between our study and Kober
399 and Craig (2016) include (but are not limited to) the magnitude of the perturbations and the time
400 variation of the perturbations. Given the lack of bias in our study, it is deemed reasonable to assess
401 member–member comparisons alongside member–control comparisons.

402 Figure 6 shows the MSD for precipitation using control–member and member–member com-
403 parisons. There is generally increasing spread in the MSD with time throughout all of the cases
404 considered. The values for MSD are similar to results obtained by Leoncini et al. (2010)³. Differ-
405 ences are apparent when comparing the evolution of the growth across the Cases A–D. Sampling
406 the ensemble members with replacement (10000 times) to produce the 5% significance level indi-

³In Leoncini et al. (2010) this diagnostic is referred to as RMSP (Root Mean Square Precipitation), and is plotted in their Figure 10.

407 cates that differences in the magnitude of the MSD, throughout the forecast, between the cases are
408 not statistically significant as there is more variation (noise) within each case than between cases.
409 However, there is a dependence of the MSD on the convective development, as to be expected from
410 Zhang et al. (2003) and Hohenegger et al. (2006). There is a clear difference in the behavior of
411 the growth of MSD. Considering the ensemble plume, Cases A and B have an initial rise and then
412 level off over the first 18 h whereas Cases C and D are more episodic, with both having at least two
413 short-timescale peaks during the increase in MSD to its overall peak value. This episodic growth
414 is tied specifically to the intensification stages of the convective events, i.e. as the event strength-
415 ens the MSD rises and thus the ensemble spread increases; conversely when the event weakens
416 the MSD falls (or stalls) and thus the ensemble spread decreases. This difference between cases
417 is also present in member–member comparisons, and when considering different thresholds for
418 precipitation (not shown). It occurs because of the different behavior of convection in the two
419 regimes. In convective quasi-equilibrium, convection is continuously being generated to maintain
420 the equilibrium. In contrast, in non-equilibrium there are periods (or places) when relatively little
421 convection is occurring prior to it being “triggered”; during such periods the growth in MSD will
422 reduce before more rapid growth occurs again when convection initiates or intensifies. This find-
423 ing is consistent with Leoncini et al. (2010) and Keil and Craig (2011) in which it was indicated
424 that convective-scale perturbation growth is larger during convective initiation. The result is also
425 robust to applying a precipitation threshold (not shown).

426 The perturbation growth is somewhat smoother when considering other variables, such as the
427 850-hPa temperature (exhibited by steadier increases in the temperature MSD compared to the
428 precipitation MSD, not shown). Nonetheless, the temporal variability makes the concept of sat-
429 uration difficult to consider in a meaningful way for the MSD diagnostic. A simple aspect of
430 perturbation growth that remains meaningful across the spectrum is the MSD doubling time (the

431 time it takes the MSD after spin-up to double). Based on the characteristics of the regimes, it
432 is hypothesized that the initial perturbation growth will be slower in the non-equilibrium events
433 (than in the equilibrium events) prior to the development of strong convection and that, once con-
434 vection has initiated, there will be greater ensemble variability in MSD doubling times for the
435 non-equilibrium events.

436 Table 1 shows the average MSD doubling time for all cases and the corresponding standard de-
437 viations in the MSD doubling time for the ensembles. The MSD doubling time is calculated from
438 fitting a straight line to the MSD of the temperature at 850 hPa starting after spin-up, and ending
439 when the growth of the MSD becomes non-linear, as in Hohenegger and Schär (2007a), using 15
440 minute data. Whilst Case A has a shorter MSD doubling time than Case D, there is no consistent
441 increase in MSD doubling time from Case A to D; this implies that the MSD doubling times are
442 not only dependent upon the convective regime. The values calculated are considerably shorter
443 than those of Hohenegger and Schär (2007a). This difference is possibly due to the higher resolu-
444 tion of our convection-permitting ensemble (1.5 km grid spacing) compared to theirs (2.2 km grid
445 spacing); although other relevant factors include the different model configurations or differences
446 in the perturbation approaches.

447 The MSD doubling times indicate a larger standard deviation (spread) for cases closer to the
448 non-equilibrium end of the spectrum (Table 1). The larger spread in doubling times implies a
449 greater spread in the ensemble (i.e. a spread in times with the same MSD value rather than a
450 spread of MSD values a specific time). The larger spread towards the non-equilibrium end of the
451 spectrum is also evident in Fig 5a, but is more evident in Fig. 5b where the standard deviation
452 of the ensemble precipitation indicates greater spread at the non-equilibrium end of the spectrum
453 (Case C and D).

454 Whilst Cases E and F are considered to be more complex, they exhibit similar values of precip-
455 itation MSD to the rest of the cases (Fig. 6). Case E shows similar behavior to that exhibited by
456 Cases C and D, by showing two short-timescale peaks during the increase in MSD to its overall
457 peak value at around 18 h, which is somewhat to be expected given the initially long τ_c . Case F
458 shows modest differences in the precipitation MSD values and spread between the periods dom-
459 inated by the front and the showers (i.e. there is only a slight increase in the standard deviation
460 for the MSD at this time; not shown). This is in contrast to an MSD computed over all points:
461 here once the front leaves the domain the MSD significantly increases as, when only showers are
462 present, the “double penalty” problem occurs (MSD for all points, not shown).

463 *b. Spatial aspects of Perturbation Growth*

464 Whilst there are differences in the perturbation growth between cases, they are relatively subtle,
465 and are not statistically significant when comparing magnitude. We now consider spatial aspects
466 of the perturbation growth. It is hypothesized, given the range of spatial scales associated with
467 convection in the different regimes, that spatial characteristics of perturbation growth will be de-
468 pendent upon the regime. This hypothesis is first considered by simple diagnosis of the fraction of
469 common points and then via the use of the FSS and dFSS.

470 When considering F_{common} across the spectrum of cases (Fig. 7) the most notable difference is the
471 localization of the perturbation growth towards the non-equilibrium end of the spectrum, indicated
472 by a larger percentage of points remaining in the same location as in the control forecast at the non-
473 equilibrium end of the spectrum. The cases towards the equilibrium end of the spectrum (Cases A
474 and B) show a rapid reduction in F_{common} with forecast lead time. In those cases F_{common} reduces to
475 around 0.20–0.25 which is close to the fraction that would be expected by pure chance, given the
476 number of precipitating points in the control forecast (red line in Fig. 7). On the other hand, the

477 cases towards the non-equilibrium end of the spectrum retain a larger fraction of common points
478 and have a large difference between that fraction and that which would be expected by chance
479 (particularly for Case C which has a fraction of approximately 0.5 common points by the end of
480 the simulation). This agreement in the positioning of convective events that show non-equilibrium
481 characteristics is consistent with Done et al. (2006) and Keil and Craig (2011), and is a result that
482 is statistically significant at the 5% significance level after bootstrapping the ensemble i.e. there is
483 no overlap of ensembles given the 5% significance level and differences between cases in different
484 regimes (Case A vs. Case D) are far larger than the variability shown by either ensemble.

485 Case D (Fig. 7d) has the longest timescale for the decay of F_{common} ; however, F_{common} at later
486 lead times becomes closer to that expected by chance than for Case C. These results are likely
487 due to there being a large spread of τ_c values across the domain in Case D (Fig. 5d), allowing
488 for some mix of growth characteristics despite the overall predominance of non-equilibrium char-
489 acteristics. The separation between F_{common} at later lead times and chance is similar in Cases B
490 and D, which may be because there is an element of local forcing involved from the orography in
491 the region where the showers are forming. The element of local forcing may improve the spatial
492 predictability for Case B, whereas the elements of the equilibrium regime limit the predictability
493 in Case D. The results also hold for member–member comparisons.

494 The cases driven by the boundary conditions (Cases E and F) show different behavior to each
495 other. Case E shows behavior similar to that of Case C in retaining a large fraction of common
496 points. This is due, in part, to the convection that is formed close to the domain boundaries
497 as the MCS enters the domain, as the lateral boundary conditions are the same in all members.
498 However, once the MCS has entered the domain, there must also be some contribution from the
499 nature of the convection itself. The fronts in Case F (Fig. 7f) have consistent positioning in the
500 perturbed members for the length of time that they remain in the domain (approximately 25 h).

501 There is a sharp drop in F_{common} at about the time the front leaves the domain, reflecting the change
502 from a frontal to an equilibrium (i.e. scattered showers) regime. As with the MSD, these results
503 for F_{common} are robust to the precipitation threshold used (not shown), thus indicating that the
504 convective regime has an influence on the spatial predictability as in Done et al. (2006, 2012).

505 The FSS and dFSS results (Fig. 8) indicate the perturbation growth across multiple scales. They
506 allow for consideration of the scale at which two forecasts agree with each other, and hence provide
507 evidence of the scale at which perturbation growth is occurring. For all of the cases there is greater
508 agreement as the neighborhood size increases and the decrease in agreement with lead time occurs
509 more rapidly at the gridscale. These are expected properties of the diagnostic (e.g. Roberts and
510 Lean 2008; Dey et al. 2014).

511 There is a clear difference in behavior between those cases closer to convective equilibrium and
512 those closer to non-equilibrium. The more equilibrium-like cases, A and B, are no longer “skill-
513 ful” at the gridscale after 13 and 9 hours, respectively. In contrast, the more non-equilibrium-like
514 case, C, remains skillful at the gridscale throughout the forecast. As in Fig. 7, Case D shows a
515 difference to Case C. Case D remains skillful until 20 hours (and does not drop far below the
516 skillful threshold, unlike Cases A and B). This is likely to be as a result of a mixture of regimes
517 across the domain. These results show that there is strong predictability in the location of pre-
518 cipitation at $O(1\text{ km})$ for the non-equilibrium-type situations, but markedly weaker predictability
519 in location of $O(10\text{ km})$ for the equilibrium-type situations. This locality of spatial predictability
520 is confirmed to be statistically significant at the 5% significance level from bootstrapping of the
521 ensemble members and no overlap occurs between the different cases in different regimes.

522 Case E also retains the gridscale predictability exhibited in Case C, which again could be partly
523 due to the MCS entering the domain through the lateral boundaries. Case F (Fig. 8f) illustrates
524 the complexity arising from an evolving synoptic situation. There is strong agreement in the

525 positioning of the front on all scales with high values of FSS, but once the front leaves the domain
526 there is a sharp reduction in the FSS implying much less agreement in the positioning of the
527 showers as the regime becomes closer to convective quasi-equilibrium.

528 As with the previous diagnostics, there is little distinction between member–member and
529 member–control forecast comparisons: the dFSS shows similar results to the FSS and the re-
530 sults are also robust to the precipitation threshold considered (not shown). Taking together Figs. 2,
531 7 and 8, we find that more organized convection (associated with the non-equilibrium regime) has
532 greater locational predictability (based on position agreement of the organized convection present
533 in Cases C–D compared to the unorganized convection in Cases A–B) and more localized per-
534 turbation growth compared to convective quasi-equilibrium cases (i.e. cell agreement is better at
535 smaller scales towards the non-equilibrium end of the spectrum, and therefore the perturbation
536 growth is more local than in equilibrium conditions). Considering also the evolution of the MSD
537 (Fig. 6), we conclude that the perturbations used have an influence on the positioning of precipita-
538 tion towards the quasi-equilibrium end of the spectrum (and hence details of location should not be
539 trusted by forecasters) and mainly on the magnitude of precipitation towards the non-equilibrium
540 end of the spectrum.

541 **5. Conclusions and Discussions**

542 Whilst convection-permitting ensembles have led to a greater understanding of convective-scale
543 predictability, the links with the synoptic-scale environment are still being uncovered. The con-
544 vective adjustment timescale is one measure for how convection links to the synoptic scale and
545 gives an indication of the convective regime. By using Gaussian perturbations inside the UKV
546 configuration of the MetUM, a convection-permitting ensemble has been generated for a spectrum
547 of convective cases including two cases driven by the boundary conditions.

548 The perturbed members produced similar precipitation distributions to each other in all cases
549 and so the perturbations did not introduce bias. There were limited differences in the magnitude of
550 the perturbation growth (which were not statistically significantly different as diagnosed from the
551 magnitude of the MSD) throughout the spectrum of convective cases considered. However, there
552 were marginally larger ensemble spreads of domain-integrated precipitation for non-equilibrium
553 events compared to the equilibrium events in agreement with Keil and Craig (2011); Done et al.
554 (2012) and Keil et al. (2014). One of the reasons for the subtle differences in the magnitude
555 of the perturbation growth between regimes, in our study compared to some previous studies, is
556 that here we consider only the common points between ensemble members and the control in
557 our precipitation MSD diagnostic. This eliminates the impact of the “double penalty” problem as
558 our MSD diagnostic measures variability in precipitation intensities only and not differences in
559 location.

560 Differences in the temperature MSD doubling times between the regimes were also somewhat
561 subtle, the non-equilibrium cases having slower growth than the equilibrium cases. However, the
562 variation in doubling times among ensemble members was somewhat larger in the non-equilibrium
563 regime. This result reflects the generally larger temporal variability for the non-equilibrium cases
564 compared with the equilibrium cases and is consistent with the expectation that convection is fairly
565 continuous in equilibrium conditions and is more sporadic for non-equilibrium conditions, early
566 on in the forecasts. This behavior further demonstrates that the perturbation growth is closely
567 dependent upon the evolution of convection in agreement with Zhang et al. (2003); Hohenegger
568 et al. (2006) and Selz and Craig (2015).

569 Whilst there are some subtle differences when considering the predictability of intensity between
570 ensemble members, the more striking (and statistically significant) differences emerge when con-
571 sidering spatial aspects of the perturbation growth. Towards the equilibrium end of the spectrum,

572 the small boundary-layer perturbations are sufficient to displace the locations of the convective
573 cells (even when there is an element of localized forcing — Case B), to an extent that approaches
574 a random relocation of the cells by the end of the forecast. This gives rise to perturbation growth
575 at scales on the order of the cloud spacing, here $O(10\text{ km})$. Towards the non-equilibrium end of
576 the spectrum, the perturbations are much less effective at displacing cells, but may perturb the de-
577 velopment of the cells. Hence, the perturbation growth is more localized to scales on the order of
578 the cell size, here $O(1\text{ km})$. These results were particularly apparent from consideration of the FSS
579 and dFSS and have implications for forecaster interpretations of convective-permitting simulations
580 such as the locations of warnings of flooding from intense rainfall events. The regime difference
581 may be due to distinct triggering mechanisms being necessary and identifiable in models in non-
582 equilibrium cases, such as localized uplift associated with convergence lines or orography (Keil
583 and Craig 2011; Keil et al. 2014). The perturbation growth for Case D presented less localization
584 than might have been anticipated given its large spatial-mean τ_c . However, the case does have a
585 relatively large spatial variation of the τ_c , suggesting a spatially-mixed regime.

586 All of the results were robust to varying the precipitation threshold. Furthermore, the conclu-
587 sions were tested against variations of the perturbation strategy including perturbations across
588 multiple vertical levels and applying spatially-correlated specific humidity and temperature per-
589 turbations. The impact of the different perturbation strategies was negligible and resulted in the
590 same conclusions as presented here (further details in Chapter 6 of Flack 2017).

591 Two complex cases were also considered that were primarily driven by the boundary conditions,
592 Cases E and F. Case E showed an initially large τ_c , but as the initiation of the event was not
593 within the domain it could not be cleanly classified into a regime. The overall characteristics
594 of the event show strong agreement in position and localization of perturbation growth. This is
595 consistent with the characteristics of a non-equilibrium event, although the results are affected by

596 the use of identical boundary conditions for all ensemble members. The second case was a frontal
597 case (Case F) and was used to determine if the simple convective regime classification remains
598 useful in more complex, spatially- and temporally-varying cases. Specifically, the presence of a
599 front dominated the precipitation pattern for the first 25 hours of the forecast and showers behind
600 the front dominated the final 11 hours. This case highlights that the simple regime classification
601 using τ_c may not provide sufficient information on the convection embedded within the front
602 because the large-scale characteristics of the front dominate the perturbation growth. However,
603 the simple regime concept became useful once the front had left the domain, since perturbation
604 growth within the post-frontal convection (which initiated inside the domain) was consistent with
605 that of the equilibrium cases considered.

606 Whilst differences in convective-scale perturbation growth are not fully described by τ_c , vari-
607 ous aspects of the spatial variability can be partially described in terms of τ_c . The relationship
608 of convective-scale perturbation growth with convective regime, particularly from the perspective
609 of spatial structure, suggests that different strategies may be preferable for prediction in the two
610 regimes. Large-member ensembles may be more valuable for forecasting events in convective
611 quasi-equilibrium due to the larger uncertainties in spatial location. The larger-member ensemble
612 will allow for more variability in position as there is little influence on the magnitude of the total
613 area-averaged precipitation (e.g. Done et al. 2006, 2012). On the other hand, higher resolution
614 forecasts may be more valuable for non-equilibrium events due to their high spatial predictability,
615 with agreement in location being retained at the kilometer scale despite boundary-layer perturba-
616 tions.

617 *Acknowledgments.* The authors would like to thank Nigel Roberts and Seonaid Dey for provid-
618 ing the FSS code and useful discussions regarding the results. The authors would also like to

619 thank the three anonymous reviewers for their comments, which have improved the manuscript.
620 The authors would also like to acknowledge the use of the MONSooN system, a collaborative
621 facility supplied under the Joint Weather and Climate Research Programme, which is a strategic
622 partnership between the Met Office and the Natural Environment Research Council (NERC). This
623 work has been funded under the work program Forecasting Rainfall Exploiting New Data Assim-
624 ilation Techniques and Novel Observations of Convection (FRANC) as part of the Flooding From
625 Intense Rainfall (FFIR) project by NERC under grant NE/K008900/1. The data used is available
626 by contacting the corresponding author.

627 **References**

- 628 Arakawa, A., and W. H. Schubert, 1974: Interaction of a Cumulus Cloud Ensemble with the Large-
629 Scale Environment, Part I. *J. Atmos. Sci.*, **31**, 674–701, doi:10.1175/1520-0469(1974)031<0674:
630 IOACCE>2.0.CO;2.
- 631 Best, M., and Coauthors, 2011: The Joint UK Land Environment Simulator (JULES), Model
632 Description–Part 1: Energy and Water Fluxes. *Geosci. Model Dev.*, **4**, 677–699, doi:10.5194/
633 gmd-4-677-2011.
- 634 Bierdel, L., P. Friederichs, and S. Bentzien, 2012: Spatial Kinetic Energy Spectra in the
635 Convection-Permitting Limited-Area NWP Model COSMO-DE. *Meteor. Z.*, **21**, 245–258, doi:
636 10.1127/0941-2948/2012/0319.
- 637 Bowler, N. E., A. Arribas, S. E. Beare, K. R. Mylne, and G. J. Shutts, 2009: The local ETKF and
638 SKEB: Upgrades to the MOGREPS Short-Range Ensemble Prediction System. *Quart. J. Roy.
639 Meteor. Soc.*, **135**, 767–776, doi:10.1002/qj.394.

- 640 Bowler, N. E., A. Arribas, K. R. Mylne, K. B. Robertson, and S. E. Beare, 2008: The MOGREPS
641 Short-Range Ensemble Prediction System. *Quart. J. Roy. Meteor. Soc.*, **134**, 703–722, doi:10.
642 1002/qj.234.
- 643 Byers, H. R., and R. R. Braham, Jr, 1948: Thunderstorm Structure and Circulation. *J. Meteor.*, **5**,
644 71–86, doi:http://dx.doi.org/10.1175/1520-0469(1948)005<0071:TSAC>2.0.CO;2.
- 645 Clark, A. J., W. A. Gallus Jr, M. Xue, and F. Kong, 2009: A Comparison of Precipitation Forecast
646 Skill Between Small Convection-Allowing and Large Convection-Parameterizing Ensembles.
647 *Wea. Forecasting*, **24**, 1121–1140, doi:10.1175/2009WAF2222318.1.
- 648 Clark, A. J., W. A. Gallus Jr, M. Xue, and F. Kong, 2010: Growth of Spread in Convection-
649 Allowing and Convection-Parameterizing Ensembles. *Wea. Forecasting*, **25**, 594–612, doi:10.
650 1175/2009WAF2222318.1.
- 651 Clark, P., N. Roberts, H. Lean, S. P. Ballard, and C. Charlton-Perez, 2016: Convection-Permitting
652 Models: A Step-Change in Rainfall Forecasting. *Meteor. Appl.*, **23**, 165–181, doi:10.1002/met.
653 1538.
- 654 Cornwall Council, 2015: Cornwall Council Flood Investigation Report. Tech. rep., Corn-
655 wall Council, 2 pp. Available online at: [https://www.cornwall.gov.uk/media/7871784/
656 Flood-investigation-report-Perranporth.pdf](https://www.cornwall.gov.uk/media/7871784/Flood-investigation-report-Perranporth.pdf).
- 657 Craig, G. C., C. Keil, and D. Leuenberger, 2012: Constraints on the Impact of Radar Rainfall Data
658 Assimilation on Forecasts of Cumulus Convection. *Quart. J. Roy. Meteor. Soc.*, **138**, 340–352,
659 doi:10.1002/qj.929.

- 660 Davies, T., M. Cullen, A. Malcolm, M. Mawson, A. Staniforth, A. White, and N. Wood, 2005: A
661 New Dynamical Core for the Met Office's Global and Regional Modelling of the Atmosphere.
662 *Quart. J. Roy. Meteor. Soc.*, **131**, 1759–1782, doi:10.1256/qj.04.101.
- 663 Dey, S. R. A., G. Leoncini, N. M. Roberts, R. S. Plant, and S. Migliorini, 2014: A Spatial View
664 of Ensemble Spread in Convection Permitting Ensembles. *Mon. Wea. Rev.*, **142**, 4091–4107,
665 doi:10.1175/MWR-D-14-00172.1.
- 666 Dey, S. R. A., N. M. Roberts, R. S. Plant, and S. Migliorini, 2016: A New Method for the Char-
667 acterization and Verification of Local Spatial Predictability for Convective-Scale Ensembles.
668 *Quart. J. Roy. Meteor. Soc.*, **142**, 1982–1996, doi:10.1002/qj.2792.
- 669 Done, J., G. Craig, S. Gray, P. Clark, and M. Gray, 2006: Mesoscale Simulations of Organized
670 Convection: Importance of Convective Equilibrium. *Quart. J. Roy. Meteor. Soc.*, **132**, 737–756,
671 doi:10.1256/qj.04.84.
- 672 Done, J., G. Craig, S. Gray, and P. A. Clark, 2012: Case-to-Case Variability of Predictability
673 of Deep Convection in a Mesoscale Model. *Quart. J. Roy. Meteor. Soc.*, **138**, 638–648, doi:
674 10.1002/qj.943.
- 675 Ebert, E. E., 2008: Fuzzy verification of high-resolution gridded forecasts: a review and proposed
676 framework. *Meteor. Appl.*, **15**, 51–64, doi:10.1002/met.25.
- 677 Edwards, J., and A. Slingo, 1996: Studies with a Flexible New Radiation Code. I: Choosing
678 a Configuration for a Large-Scale Model. *Quart. J. Roy. Meteor. Soc.*, **122**, 689–719, doi:10.
679 1002/qj.49712253107.
- 680 Emanuel, K. A., 1994: *Atmospheric Convection*. Oxford University Press, 580 pp.

- 681 Flack, D. L. A., 2017: Environmental Controls on Convective-Scale Perturbation Growth. Ph.D.
682 thesis, University of Reading, 146 pp.
- 683 Flack, D. L. A., R. S. Plant, S. L. Gray, H. W. Lean, C. Keil, and G. C. Craig, 2016: Characterisa-
684 tion of Convective Regimes over the British Isles. *Quart. J. Roy. Meteor. Soc.*, **142**, 1541–1553,
685 doi:10.1002/qj.2758.
- 686 Hohenegger, C., D. Lüthi, and C. Schär, 2006: Predictability Mysteries in Cloud-Resolving Mod-
687 els. *Mon. Wea. Rev.*, **134**, 2095–2107, doi:10.1175/MWR3176.1.
- 688 Hohenegger, C., and C. Schär, 2007a: Atmospheric Predictability at Synoptic versus Cloud-
689 Resolving Scales. *Bull. Amer. Meteor. Soc.*, **88**, 1783–1793, doi:10.1175/BAMS-88-11-1783.
- 690 Hohenegger, C., and C. Schär, 2007b: Predictability and Error Growth Dynamics in Cloud-
691 Resolving Models. *J. Atmos. Sci.*, **64**, 4467–4478, doi:10.1175/2007JAS2143.1.
- 692 Johnson, A., and X. Wang, 2016: A Study of Multiscale Initial Condition Perturbation Methods
693 for Convection-Permitting Ensemble Forecasts. *Mon. Wea. Rev.*, **144**, 2579–2604, doi:10.1175/
694 MWR-D-16-0056.1.
- 695 Johnson, A., and Coauthors, 2014: Multiscale Characteristics and Evolution of Perturbations for
696 Warm Season Convection-Allowing Precipitation Forecasts: Dependence on Background Flow
697 and Method of Perturbation. *Mon. Wea. Rev.*, **142**, 1053–1073, doi:10.1175/MWR-D-13-00204.
698 1.
- 699 Keil, C., and G. C. Craig, 2011: Regime-Dependent Forecast Uncertainty of Convective Precipi-
700 tation. *Meteor. Z.*, **20**, 145–151, doi:10.1127/0941-2948/2011/0219.

- 701 Keil, C., F. Heinlein, and G. Craig, 2014: The Convective Adjustment Time-scale as Indicator
702 of Predictability of Convective Precipitation. *Quart. J. Roy. Meteor. Soc.*, **140**, 480–490, doi:
703 10.1002/qj.2143.
- 704 Kober, K., and G. C. Craig, 2016: Physically-based Stochastic Perturbations (PSP) in the Bound-
705 ary Layer to Represent Uncertainty in Convective Initiation. *J. Atmos. Sci.*, **73**, 2893–2911,
706 doi:10.1175/JAS-D-15-0144.1.
- 707 Kühnlein, C., C. Keil, G. Craig, and C. Gebhardt, 2014: The Impact of Downscaled Initial Con-
708 dition Perturbations on Convective-Scale Ensemble Forecasts of Precipitation. *Quart. J. Roy.*
709 *Meteor. Soc.*, **140**, 1552–1562, doi:10.1002/qj.2238.
- 710 Lean, H. W., P. A. Clark, M. Dixon, N. M. Roberts, A. Fitch, R. Forbes, and C. Halli-
711 well, 2008: Characteristics of High-Resolution Versions of the Met Office Unified Model
712 for Forecasting Convection Over the United Kingdom. *Mon. Wea. Rev.*, **136**, 3408–3424, doi:
713 10.1175/2008MWR2332.1.
- 714 Leicestershire County Council, 2014: Market Harborough Flood Report. Tech. rep., Leicestershire
715 County Council, 35 pp. Available online at: [http://www.leicestershire.gov.uk/sites/default/files/
716 field/pdf/2016/9/19/market_harborough_tc_detailed_flood_investigation_final.pdf](http://www.leicestershire.gov.uk/sites/default/files/field/pdf/2016/9/19/market_harborough_tc_detailed_flood_investigation_final.pdf).
- 717 Leon, D. C., and Coauthors, 2016: The Convective Precipitation Experiment (COPE): Investi-
718 gating the Origins of Heavy Precipitation in the Southwestern United Kingdom. *Bull. Amer.*
719 *Meteor. Soc.*, **97**, 1003–1020, doi:10.1175/BAMS-D-14-00157.1.
- 720 Leoncini, G., R. Plant, S. Gray, and P. Clark, 2010: Perturbation Growth at the Convective Scale
721 for CSIP IOP8. *Quart. J. Roy. Meteor. Soc.*, **136**, 653–670, doi:10.1002/qj.587.

- 722 Leoncini, G., R. Plant, S. Gray, and P. Clark, 2013: Ensemble Forecasts of a Flood-Producing
723 Storm: Comparison of the Influence of Model-State Perturbations and Parameter Modifications.
724 *Quart. J. Roy. Meteor. Soc.*, **139**, 198–211, doi:10.1002/qj.1951.
- 725 Lock, A., A. Brown, M. Bush, G. Martin, and R. Smith, 2000: A New Boundary Layer Mixing
726 Scheme. Part I: Scheme Description and Single-Column Model Tests. *Mon. Wea. Rev.*, **128**,
727 3187–3199, doi:10.1175/1520-0493(2000)128<3187:ANBLMS>2.0.CO;2.
- 728 Lorenz, E. N., 1969: The Predictability of a Flow which Possesses Many Scales of Motion. *Tellus*,
729 **21**, 289–307, doi:10.1111/j.2153-3490.1969.tb00444.x.
- 730 McCabe, A., R. Swinbank, W. Tennant, and A. Lock, 2016: Representing Model Uncertainty
731 in the Met Office Convection-Permitting Ensemble Prediction System and its Impact on Fog
732 Forecasting. *Quart. J. Roy. Meteor. Soc.*, **142**, 2897–2910, doi:10.1002/qj.2876.
- 733 Melhauser, C., and F. Zhang, 2012: Practical and Intrinsic Predictability of Severe and Convective
734 Weather at the Mesoscales. *J. Atmos. Sci.*, **69**, 3350–3371, doi:10.1175/JAS-D-11-0315.1.
- 735 Mittermaier, M. P., 2014: A Strategy for Verifying Near-Convection-Resolving Model Forecasts
736 at Observing Sites. *Wea. Forecasting*, **29**, 185–204, doi:10.1175/WAF-D-12-00075.1.
- 737 Molini, L., A. Parodi, N. Rebora, and G. Craig, 2011: Classifying Severe Rainfall Events over
738 Italy by Hydrometeorological and Dynamical Criteria. *Quart. J. Roy. Meteor. Soc.*, **137**, 148–
739 154, doi:10.1002/qj.741.
- 740 Nottingham City Council, 2015: Flood Investigation Report 23 July 2013 Flood Event
741 Winchester Street, Spondon Street and Haydn Road, Sherwood, Nottingham. Tech. rep.,
742 Nottingham City Council, 38 pp. Available online at: [http://www.nottinghamcity.gov.uk/
743 environmental-health-and-safer-housing/safer-housing/lead-local-flood-authority/](http://www.nottinghamcity.gov.uk/environmental-health-and-safer-housing/safer-housing/lead-local-flood-authority/).

744 Raynaud, L., and F. Bouttier, 2015: Comparison of Initial Perturbation Methods for Ensemble
745 Prediction at Convective Scale. *Quart. J. Roy. Meteor. Soc.*, **142**, 854–866, doi:10.1002/qj.2686.

746 Roberts, N. M., and H. W. Lean, 2008: Scale-Selective Verification of Rainfall Accumulations
747 from High-Resolution Forecasts of Convective Events. *Mon. Wea. Rev.*, **136**, 78–97, doi:10.
748 1175/2007MWR2123.1.

749 Selz, T., and G. C. Craig, 2015: Upscale Error Growth in a High-Resolution Simulation of
750 a Summertime Weather Event over Europe. *Mon. Wea. Rev.*, **143**, 813–827, doi:10.1175/
751 MWR-D-14-00140.1.

752 Stein, T. H., R. J. Hogan, P. A. Clark, C. E. Halliwell, K. E. Hanley, H. W. Lean, J. C. Nicol,
753 and R. S. Plant, 2015: The DYMECS project: A Statistical Approach for the Evaluation of
754 Convective Storms in High-Resolution NWP Models. *Bull. Amer. Meteor. Soc.*, **96**, 939–951,
755 doi:10.1175/BAMS-D-13-00279.1.

756 Surcel, M., I. Zawadzki, and M. K. Yau, 2016: The Case-to-Case Variability of the Predictability
757 of Precipitation by a Storm-Scale Ensemble Forecasting System. *Mon. Wea. Rev.*, **144**, 193–212,
758 doi:10.1175/MWR-D-15-0232.1.

759 Tang, Y., H. W. Lean, and J. Bornemann, 2013: The Benefits of the Met Office Variable Resolution
760 NWP Model for Forecasting Convection. *Meteor. Appl.*, **20**, 417–426, doi:10.1002/met.1300.

761 Verrelle, A., D. Ricard, and C. Lac, 2015: Sensitivity of High-Resolution Idealized Simulations of
762 Thunderstorms to Horizontal Resolution and Turbulence Parametrization. *Quart. J. Roy. Meteor.
763 Soc.*, **141**, 433–448, doi:10.1002/qj.2363.

- 764 Wilson, D. R., and S. P. Ballard, 1999: A Microphysically Based Precipitation Scheme for the
765 UK Meteorological Office Unified Model. *Quart. J. Roy. Meteor. Soc.*, **125**, 1607–1636, doi:
766 10.1002/qj.49712555707.
- 767 Wood, N., and Coauthors, 2014: An Inherently Mass-Conserving Semi-Implicit Semi-Lagrangian
768 Discretisation of the Deep-Atmosphere Global Nonhydrostatic Equations. *Quart. J. Roy. Me-
769 teor. Soc.*, **140**, 1505–1520, doi:10.1002/qj.2235.
- 770 Wyngaard, J. C., and O. R. Cot, 1971: The Budgets of Turbulent Kinetic Energy and Temper-
771 ature Variance in the Atmospheric Surface Layer. *J. Atmos. Sci.*, **28**, 190–201, doi:10.1175/
772 1520-0469(1971)028<0190:TBOTKE>2.0.CO;2.
- 773 Xue, M., J. Schleif, F. Kong, K. W. Thomas, Y. Wang, and K. Zhu, 2013: Track and Intensity
774 Forecasting of Hurricanes: Impact of Convection-Permitting Resolution and Global Ensemble
775 Kalman Filter Analysis on 2010 Atlantic Season Forecasts. *Wea. Forecasting*, **28**, 1366–1384,
776 doi:10.1175/WAF-D-12-00063.1.
- 777 Zhang, F., N. Bei, R. Rotunno, C. Snyder, and C. C. Epifanio, 2007: Mesoscale Predictability
778 of Moist Baroclinic Waves: Convection-Permitting Experiments and Multistage Error Growth
779 Dynamics. *J. Atmos. Sci.*, **64**, 3579–3594, doi:10.1175/JAS4028.1.
- 780 Zhang, F., C. Snyder, and R. Rotunno, 2003: Effects of Moist Convection on Mesoscale Pre-
781 dictability. *J. Atmos. Sci.*, **60**, 1173–1185, doi:10.1175/1520-0469(2003)060<1173:EOMCOM>
782 2.0.CO;2.
- 783 Zimmer, M., G. Craig, C. Keil, and H. Wernli, 2011: Classification of Precipitation Events with a
784 Convective Response Timescale and their Forecasting Characteristics. *Geophys. Res. Lett.*, **38**,
785 doi:10.1029/2010GL046199.

786 **LIST OF TABLES**

787 **Table 1.** Average doubling times for the spectrum of cases with standard deviation, cal-
788 culated from the MSD of temperature at approximately 850 hPa. 38

789 TABLE 1. Average doubling times for the spectrum of cases with standard deviation, calculated from the MSD
790 of temperature at approximately 850 hPa.

Date	Doubling Time (minutes)	Standard Deviation (minutes)
Case A	19.2	0.3
Case B	27.0	0.5
Case C	23.6	0.7
Case D	36.3	3.4
Case E	28.3	2.8
Case F	18.4	0.6

791 **LIST OF FIGURES**

792 **Fig. 1.** Met Office surface analyses for 1200 UTC on a) 20 April 2012, b) 12 August 2013, c)
793 23 July 2013, d) 2 August 2013, e) 27 July 2013 and f) 5 August 2013. The figure panel
794 labels refer to their respective cases (e.g. panel a is for Case A). Courtesy of the Met Office
795 (©British Crown Copyright, Met Office 2012, 2013). 41

796 **Fig. 2.** A summary of the ensemble hourly precipitation accumulations greater than 1 mm given by
797 the number of perturbed ensemble members precipitating at that point in the domain (color
798 bar). The mean sea level pressure from the control forecast is also shown (4 hPa contour
799 interval). Each plot is for 1200 UTC and the blue line in b) represents a distance of 100 km.
800 Each panel refers to the respective case. 42

801 **Fig. 3.** The average hourly convective adjustment timescale over a coarse-grained UKV domain.
802 Each line represents a different case: A (blue, asterisk), B (purple, cross), C (orange, circle),
803 D (maroon, plus), E (pink, circle) and F (black). The missing section for Case F is due
804 to τ_c being undefined as the precipitation did not meet the required threshold to enable τ_c
805 to be calculated. The vertical dot-dashed line at three hours denotes the spin-up time, the
806 horizontal dashed lines at three hours denotes the threshold time, and the symbols ' $i\chi$ ' mark
807 convective initiation times as described in the main text, where χ denotes case letter. All
808 values are plotted at half past the hour. 43

809 **Fig. 4.** Maps of the convective adjustment timescale for Cases A–D at 1500 UTC on the case day. . . . 44

810 **Fig. 5.** A summary of the ensemble convective precipitation as a function of lead time, with all
811 forecasts initiated at 0000 UTC: a) the domain-average hourly-accumulations over all points
812 in the domain and b) the corresponding standard deviation. The thick line represents the
813 control and the dashed lines represent the perturbed members: Case A (blue, asterisk), B
814 (purple, cross), C (orange, circles), D (maroon, plus), E (pink, diamonds) and F (black).
815 The vertical dashed line at three hours denotes the spin-up time, and all values are plotted at
816 half past the hour. 45

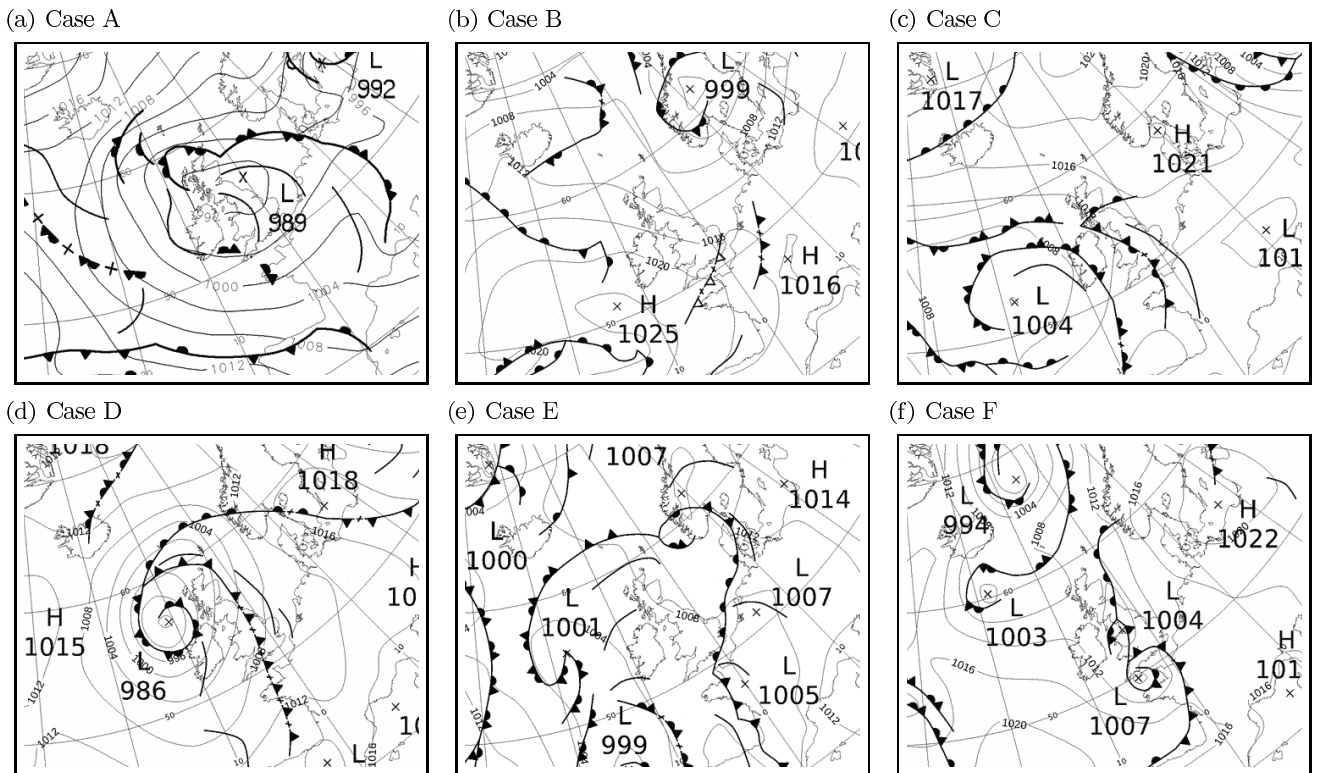
817 **Fig. 6.** The normalized mean square difference (MSD) for precipitation as a function of lead time for
818 Cases A–F. The dark blue lines represent control–member comparisons and the dashed gray
819 lines represent member–member comparisons. The spikes in b) just after 24 hours reach 1.4
820 and 1.5 respectively. The dashed line at 3 hours represents the spin-up time and the dot-dash
821 line at 25 hours on f) represents the time when the front has completely left the domain in
822 all ensemble members. All values are plotted at half past the hour. 46

823 **Fig. 7.** The fraction of points that have hourly precipitation accumulations greater than 1 mm at
824 the same position in both forecasts (F_{common}) considered as a function of forecast time for
825 Cases A–F: the dark blue lines represent control–member comparisons and dashed gray
826 lines represent member–member comparisons. The dashed line at 3 hours represents the
827 spin-up time and the dot-dash line at 25 hours on f) represents the time when the front has
828 completely left the domain in all ensemble members. The red line on all panels represents
829 the fraction of points that would be the same in both forecasts through chance based on the
830 number of precipitating points in the control forecast. All values are plotted at half past the
831 hour. 47

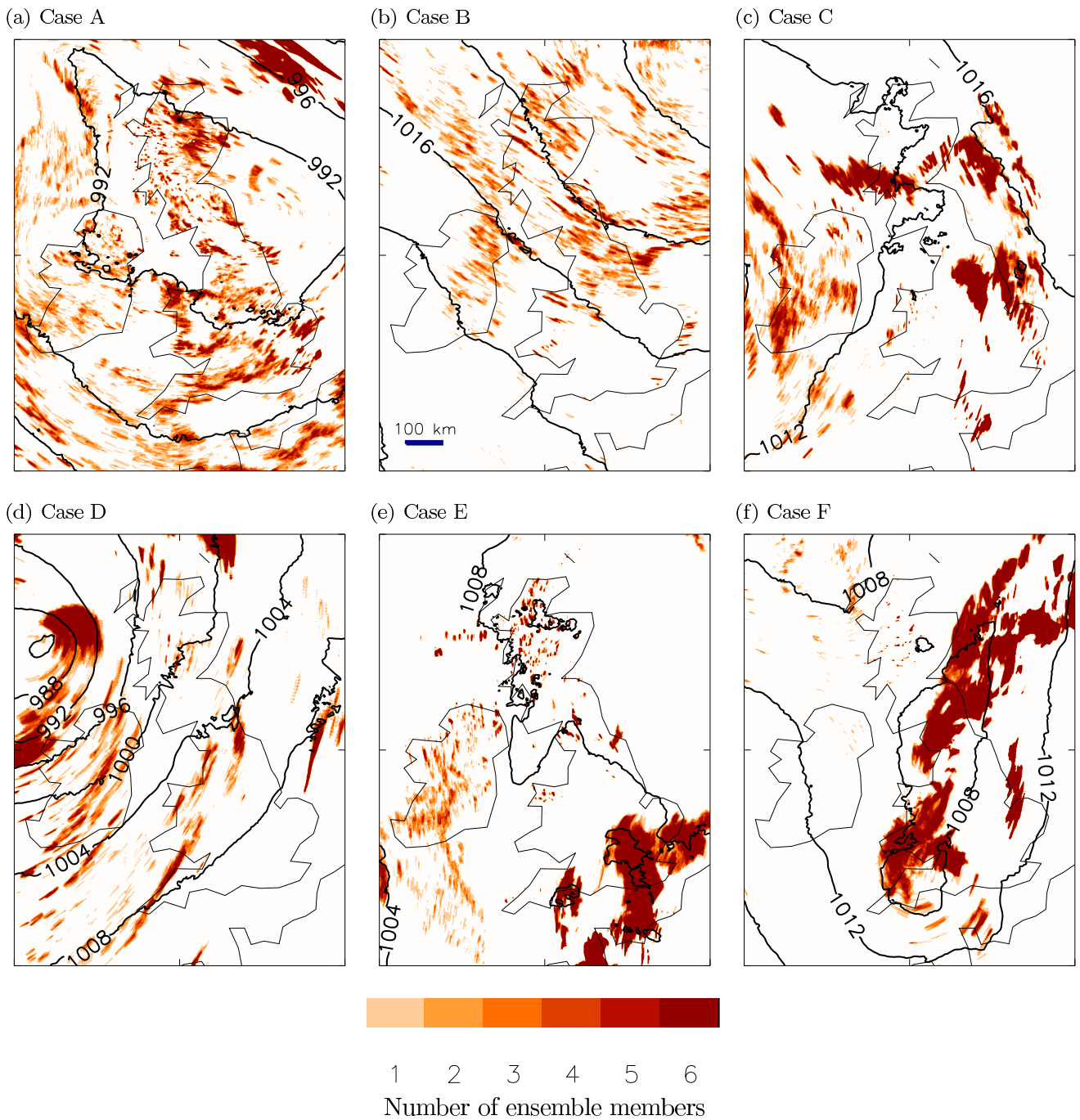
832 **Fig. 8.** The Fractions Skill Score (FSS) between runs for hourly accumulations with a threshold of
833 1 mm as a function of time, for Cases A–F. The black lines represent the FSS at the grid-
834 scale, the blue lines represents a neighborhood width of 10.5 km, the purple a neighborhood
835 width of 31.5 km and the green a neighborhood width of 61.5 km. The dashed red line (FSS

836
837
838
839
840
841
842

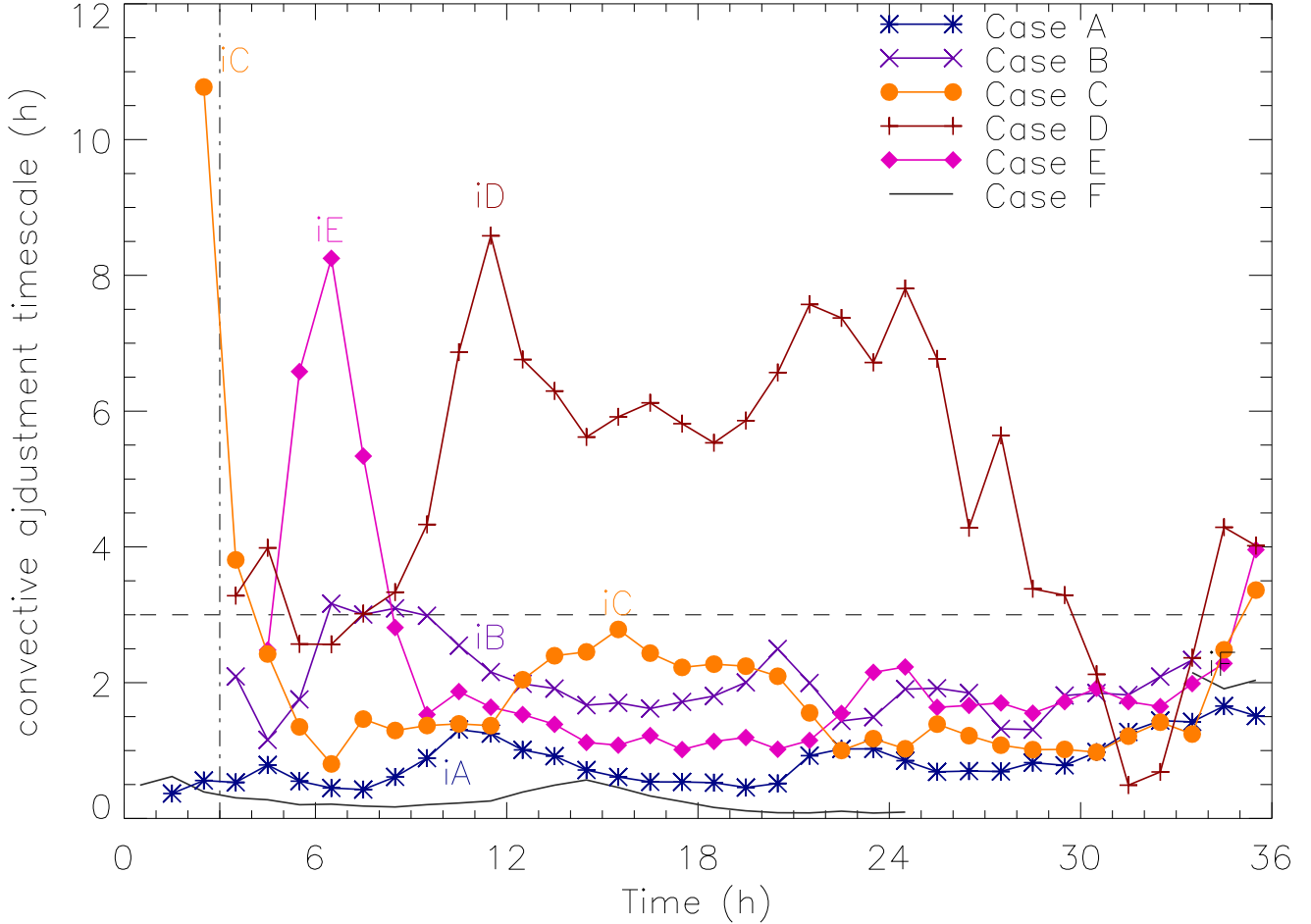
= 0.5) represents the separation between a skillful forecast with respect to the comparison run and not: those neighborhoods with an FSS greater than 0.5 are considered to have locational predictability, and those with an FSS less than 0.5 are considered to be unpredictable (in terms of location). The paler dashed lines represent member–member comparisons, with the vertical dot-dashed line representing the spin-up time and the dot-dot-dot-dash line representing the time the front leaves the domain for Case F. All values are plotted at half past the hour. 48



843 FIG. 1. Met Office surface analyses for 1200 UTC on a) 20 April 2012, b) 12 August 2013, c) 23 July 2013,
 844 d) 2 August 2013, e) 27 July 2013 and f) 5 August 2013. The figure panel labels refer to their respective cases
 845 (e.g. panel a is for Case A). Courtesy of the Met Office (©British Crown Copyright, Met Office 2012, 2013).

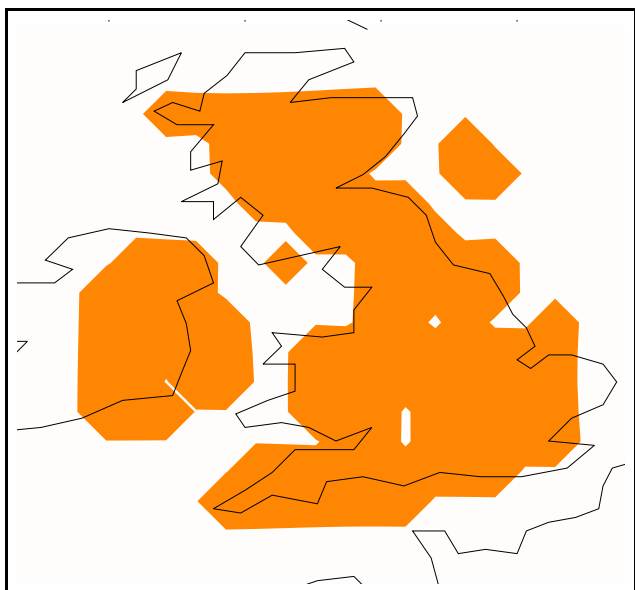


846 FIG. 2. A summary of the ensemble hourly precipitation accumulations greater than 1 mm given by the
 847 number of perturbed ensemble members precipitating at that point in the domain (color bar). The mean sea level
 848 pressure from the control forecast is also shown (4 hPa contour interval). Each plot is for 1200 UTC and the
 849 blue line in b) represents a distance of 100 km. Each panel refers to the respective case.

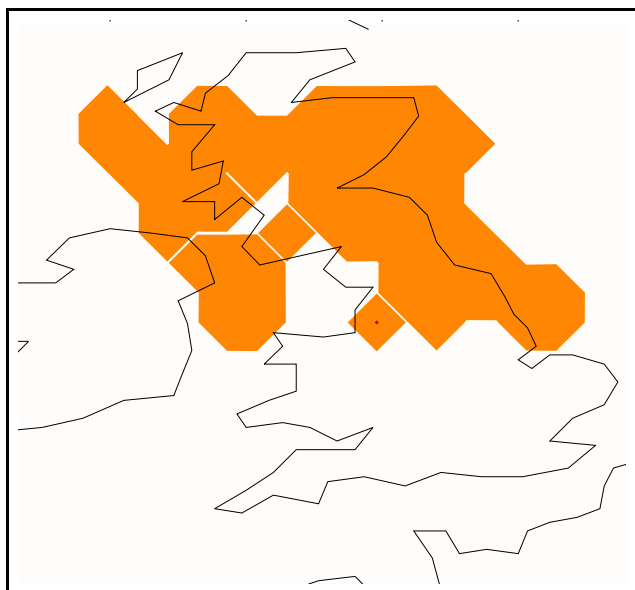


850 FIG. 3. The average hourly convective adjustment timescale over a coarse-grained UKV domain. Each line
 851 represents a different case: A (blue, asterisk), B (purple, cross), C (orange, circle), D (maroon, plus), E (pink,
 852 circle) and F (black). The missing section for Case F is due to τ_c being undefined as the precipitation did not
 853 meet the required threshold to enable τ_c to be calculated. The vertical dot-dashed line at three hours denotes the
 854 spin-up time, the horizontal dashed lines at three hours denotes the threshold time, and the symbols 'i χ ' mark
 855 convective initiation times as described in the main text, where χ denotes case letter. All values are plotted at
 856 half past the hour.

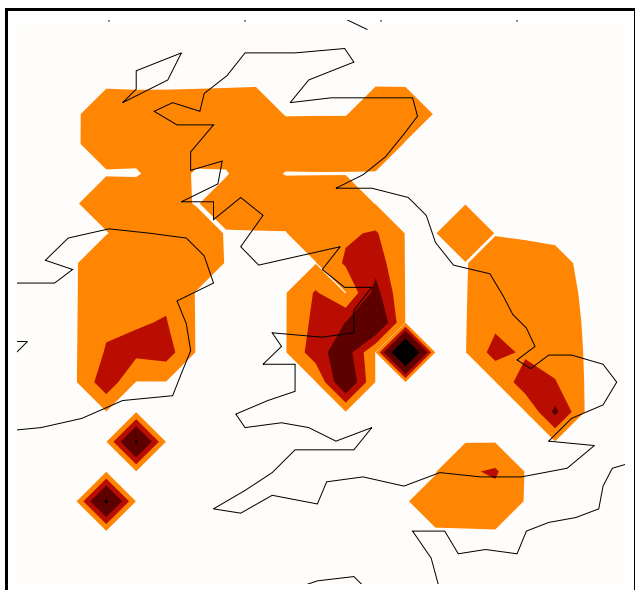
(a) Case A



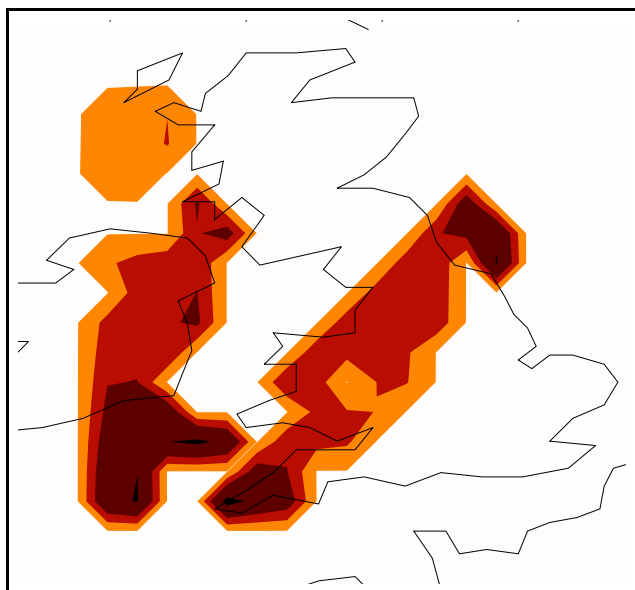
(b) Case B



(c) Case C



(d) Case D

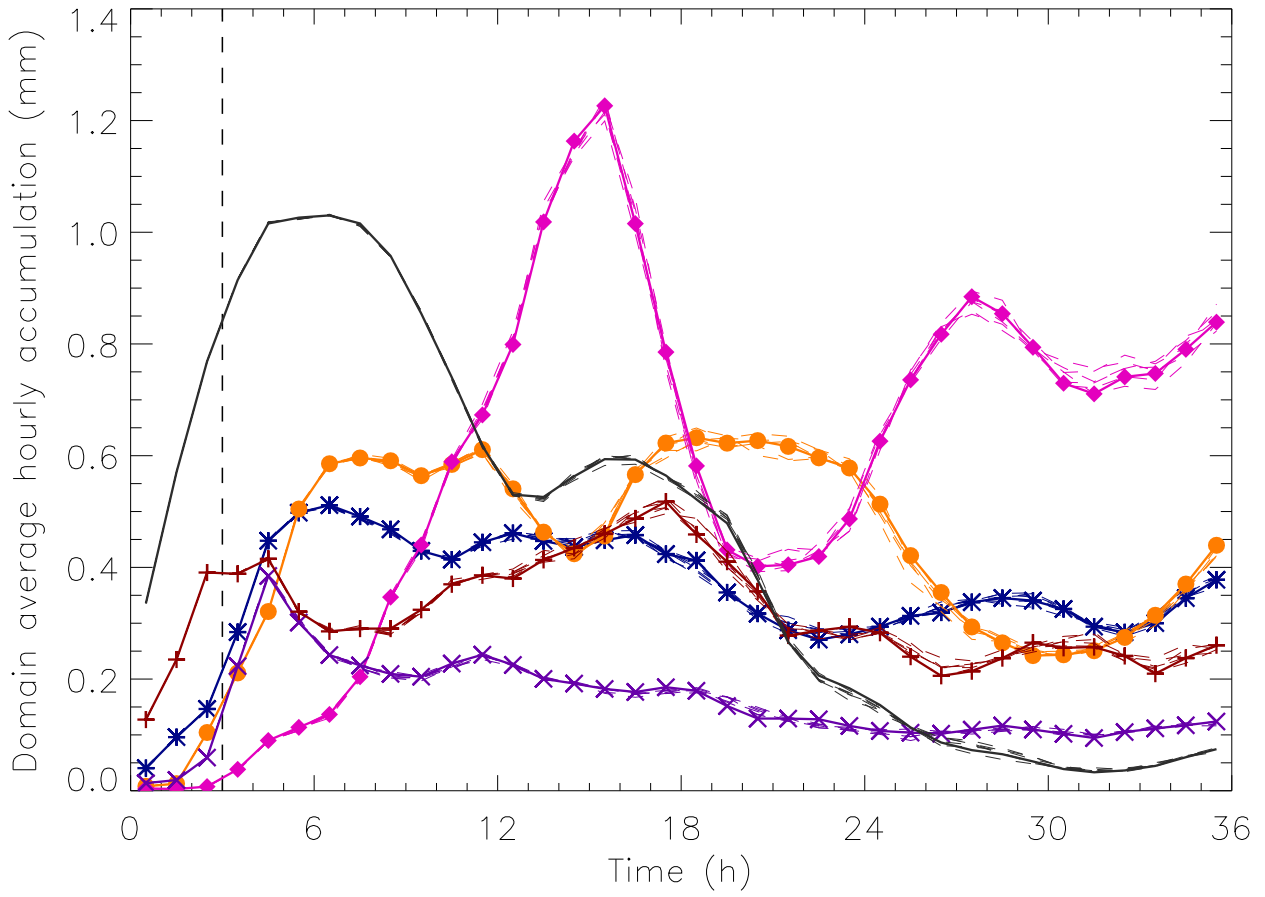


0 3 6 12

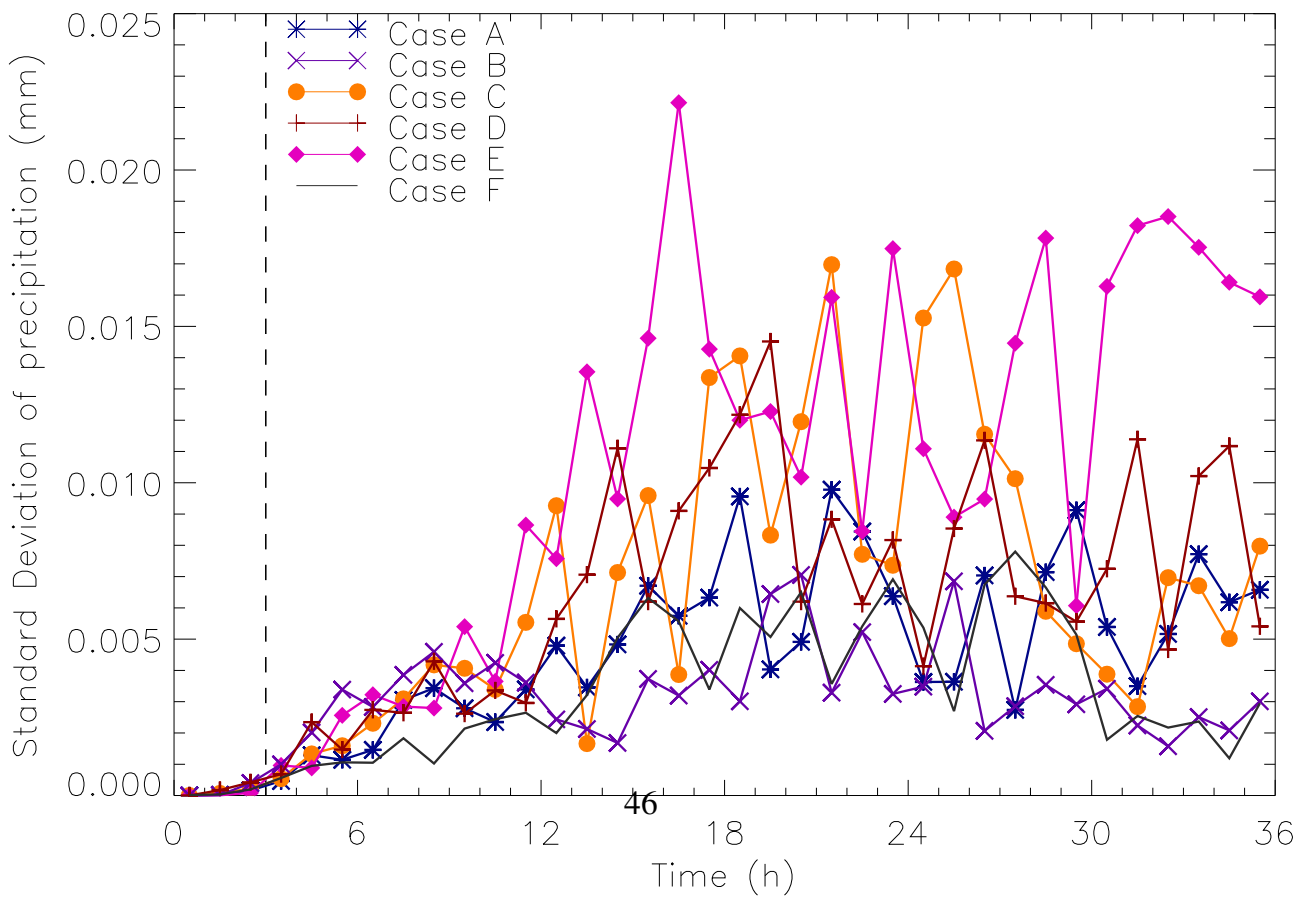
τ_c (h)

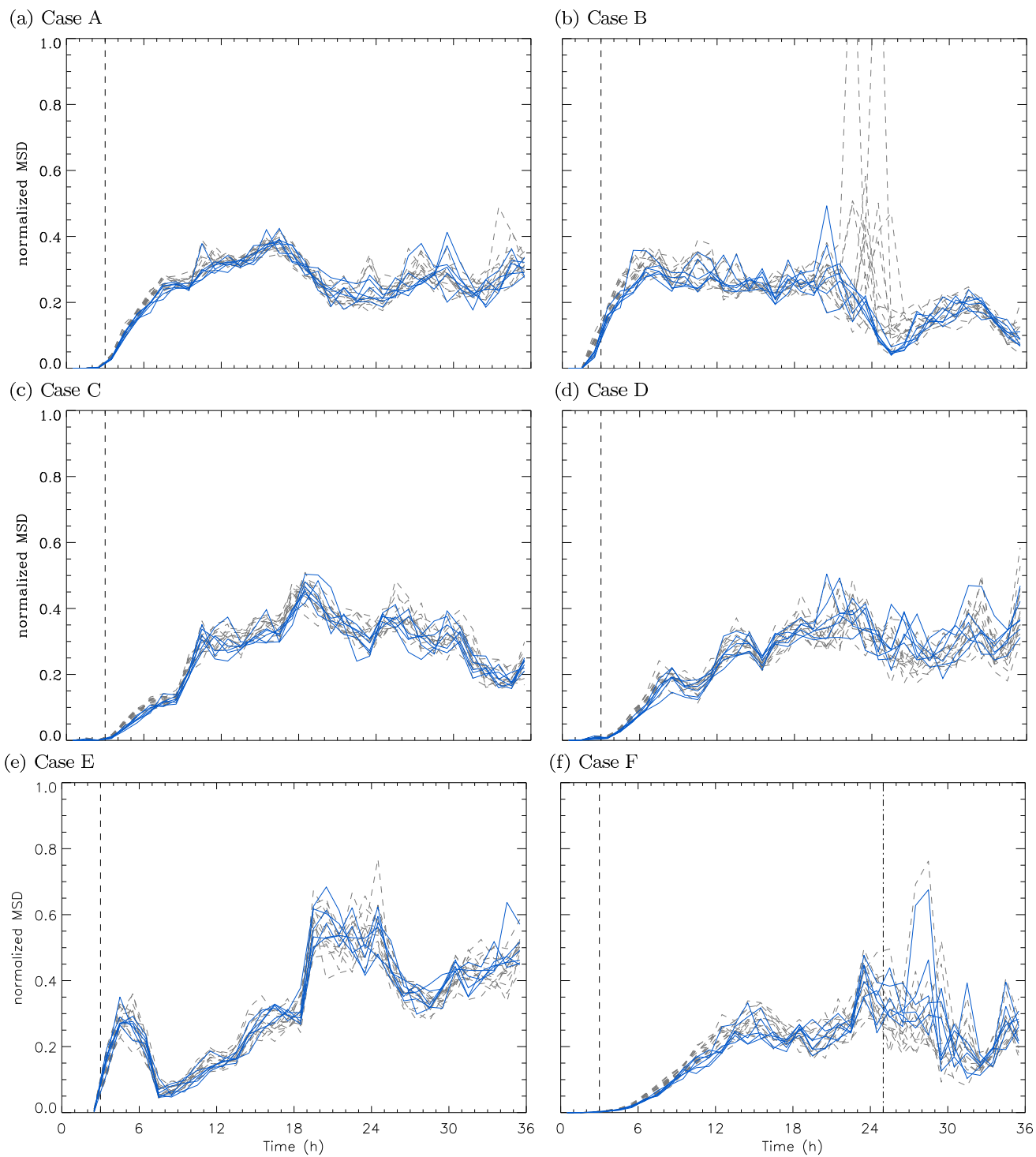
FIG. 4. Maps of the convective adjustment timescale for Cases A–D at 1500 UTC on the case day.

(a)

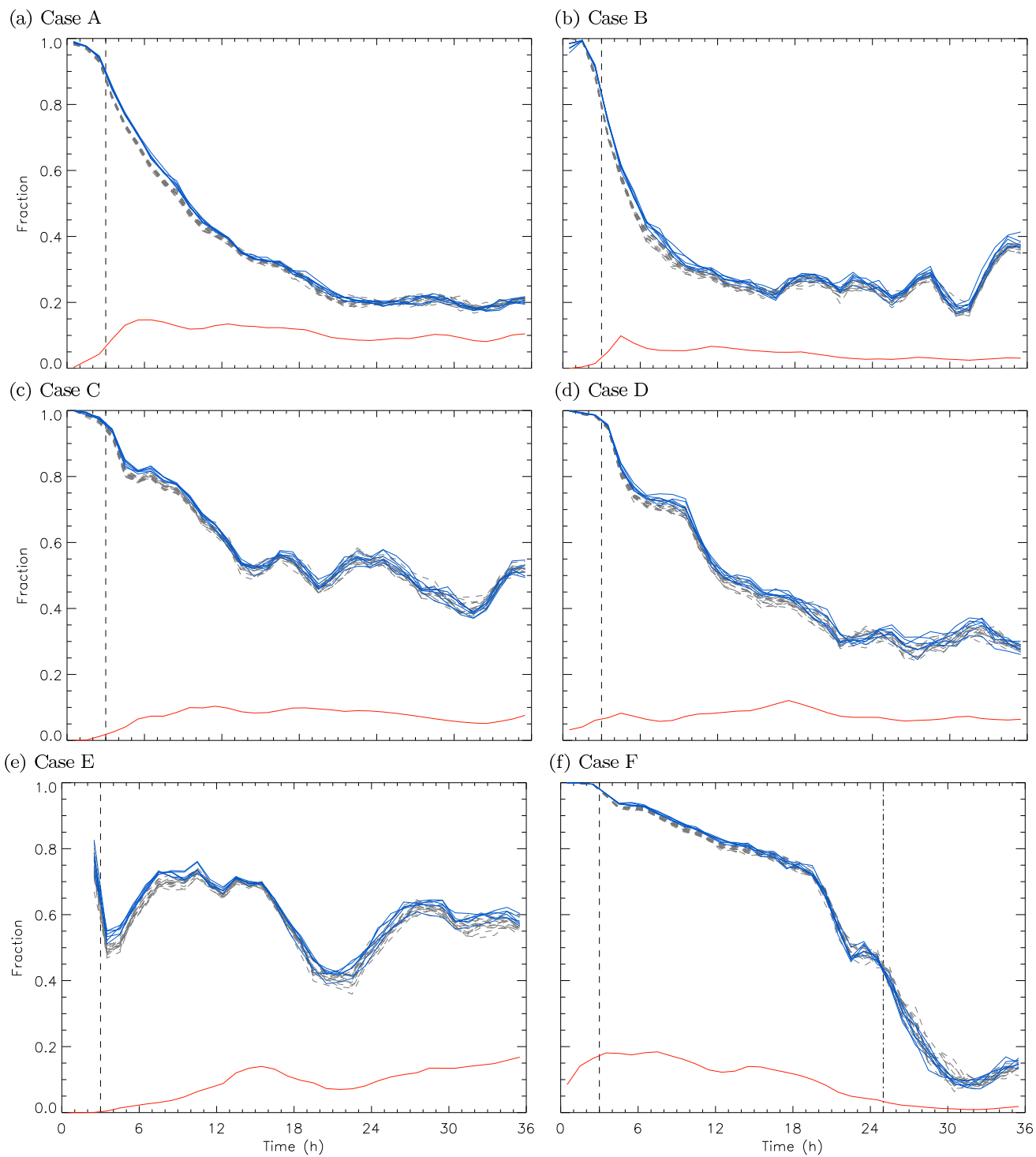


(b)

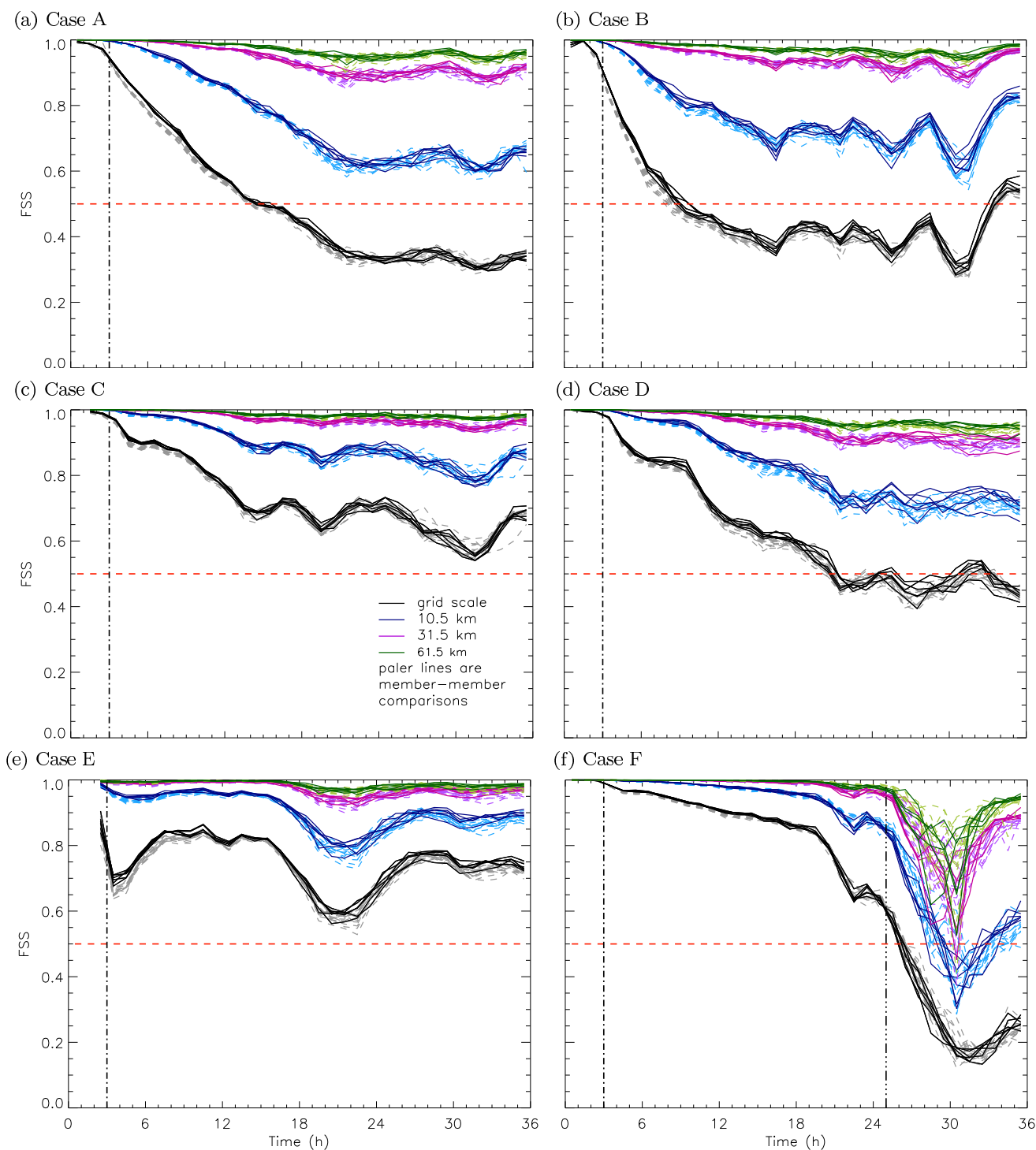




863 FIG. 6. The normalized mean square difference (MSD) for precipitation as a function of lead time for Cases
 864 A–F. The dark blue lines represent control–member comparisons and the dashed gray lines represent member–
 865 member comparisons. The spikes in b) just after 24 hours reach 1.4 and 1.5 respectively. The dashed line at
 866 3 hours represents the spin-up time and the dot-dash line at 25 hours on f) represents the time when the front has
 867 completely left the domain in all ensemble members. All values are plotted at half past the hour.



868 FIG. 7. The fraction of points that have hourly precipitation accumulations greater than 1 mm at the same
 869 position in both forecasts (F_{common}) considered as a function of forecast time for Cases A–F: the dark blue lines
 870 represent control–member comparisons and dashed gray lines represent member–member comparisons. The
 871 dashed line at 3 hours represents the spin-up time and the dot-dash line at 25 hours on f) represents the time
 872 when the front has completely left the domain in all ensemble members. The red line on all panels represents the
 873 fraction of points that would be the same in both forecasts through chance based on the number of precipitating
 874 points in the control forecast. All values are plotted at half past the hour.



875 FIG. 8. The Fractions Skill Score (FSS) between runs for hourly accumulations with a threshold of 1 mm as
876 a function of time, for Cases A–F. The black lines represent the FSS at the gridscale, the blue lines represents
877 a neighborhood width of 10.5 km, the purple a neighborhood width of 31.5 km and the green a neighborhood
878 width of 61.5 km. The dashed red line (FSS = 0.5) represents the separation between a skillful forecast with
879 respect to the comparison run and not: those neighborhoods with an FSS greater than 0.5 are considered to
880 have locational predictability, and those with an FSS less than 0.5 are considered to be unpredictable (in terms
881 of location). The paler dashed lines represent member–member comparisons, with the vertical dot-dashed line
882 representing the spin-up time and the dot-dot-dot-dash line representing the time the front leaves the domain for